Results from the last DD and DT JET campaigns in the framework of the EUROfusion Tokamak Exploitation Work Package activity

PAPER • OPEN ACCESS

Results from the last DD and DT JET campaigns in the framework of the EUROfusion Tokamak Exploitation Work Package activity

To cite this article: N. Vianello *et al* 2026 *Nucl. Fusion* **66** 116010

OPEN ACCESS
IOP Publishing | International Atomic Energy Agency
Nuclear Fusion
Nucl. Fusion **66** (2026) 116010 (31pp)
https://doi.org/10.1088/1741-4326/ae71ec

Results from the last DD and DT JET campaigns in the framework of the EUROfusion Tokamak Exploitation Work Package activity

N. Vianello[1,2,*], E. Joffrin[3], M. Baruzzo[1,4], A. Hakola[5], A. Kappatou[6], D. Keeling[7], B. Labit[8], E. Tsitrone[3], M. Wischmeier[6], J. Adamek[9], M. Agostini[1,2], C. Albert[10], F.C.P. Albert Devasagayam[11], G. Alberti[12], F. Albrecht[6], S. Aleiferis[7,13], E. Alessi[14], J. Alhage[15], S. Allan[7], M. Alonzo[16], S. An[6], G. Anastasiou[13], E. Andersson-Sunden[17], C. Angioni[6], F. Antlitz[6], Y. Antonenas[13], G.M. Apruzzese[16], M. Ariola[18], J.F. Artaud[3], W. Arter[7], A. Ash[7], Y. Asnis[8], O. Asztalos[19], L. Aucone[20], M.H. Aumeunier[3], F. Auriemma[1,2], C. Avanzato[21], J. Ayllon-Guerola[22], E. Aymerich[23], A. Baciero[24], F. Bairaktaris[13], P. Balázs[19], L. Balbinot[21], I. Balboa[7], A. Balestri[8], O. Bardsley[7], A. Battey[8], T. Bauer[25], C. Baumann[26], M.G. Bergmann[6], H. Bergstroem[6], E. Bernard[3], M. Bernert[6], A. Biancalani[27], R. Bianchetti Morales[7], R. Bilato[6], P. Bilkova[9], W. Bin[14], G. Birkenmeier[6], R. Bisson[28], S. Blackmore[7], F. Blaise[29], V. Bobkov[6], A. Boboc[7], A. Bock[6], P. Bohm[9], T. Bolzonella[1], L. Bonalumi[14], D. Bonfiglio[1,2], M. Bonisolli[8], D. Borodin[26], I. Borodkina[9], T. Bosman[30], C. Bottereau[3], L. Bramucci[1], B. Brandström[31], S. Brezinsek[26], D. Brida[6], M. Brix[7], F. Brochard[32], B. Brown[8], A. Bruncrona[5], D. Brunetti[7], J. Bryant[7], J. Buermans[33], H. Bufferand[3], A. Burckhart[6], J. Cai[26], J. Caloud[9], G. Camera[18], F. Cani[2], B. Cannas[23], P. Cano Megias[22], M. Cappelli[16], A. Cardinali[16], S. Carli[34], D. Carnevale[35], M. Carpita[8], P. Carvalho[7], A. Casolari[9], F. Casson[7], C. Castaldo[16], R. Castro[24], A. Cathey[6], F. Causa[14], J. Cavalier[9], M. Cavedon[20], J. Cazabonne[3], M. Cecconello[17], L. Ceelen[30], A. Celora[20], J. Cerovsky[9], C. Challis[7], R. Chandra[11], B. Chapman-Oplopoiou[7], O. Chellai[8], X. Chen[36], M. Chernyshova[37], J. Chlum[9], P. Chmielewski[37], A. Chomiczewska[37], F. Cichocki[16], R. Cicioni[1], A. Cioffi[38], G. Ciraolo[3], S. Ciufo[1], A. Ciurlino[20], A. Civit[39], F. Clairet[3], A. Clod[40], S. Coda[8], R. Coelho[41], I. Coffey[7], L. Colas[3], S. Conroy[17], C. Contre[8], N. Conway[7], R. Coosemans[8], L. Cordaro[1], M. Cornelissen[30], Y. Corre[3], Š. Costea[42], X. Courtois[3], T. Craciunescu[43], G. Croci[20], K. Crombe[33], D.J. Cruz Zabala[22], F. Cursi[34], M. Czarski[37], T. Czarski[37], F.A. D'Isa[1], M. Dalla Rosa[20], M. Damiano[35], M. De Angeli[14], E. de la Cal[24], E. De La Luna[24], G. De Masi[1,2], C. De Piccoli[1], J. De Rycke[15], G. De Tommasi[18], J. Decker[8], R. Dejarnac[9], W. Dekeyser[34], D. Del Sarto[32], E. Delabie[44], J. Denis[28], G. Derks[30], C. Desgranges[3], E. Devlaminck[8], P. Devynck[3], L.E. di Grazia[18], C. Di Troia[16], M. Dicorato[6], M. Diez[3], V. Dimitriou[45], M. Dimitrova[9], T. Dittmar[26], L. Dittrich[6], D. Grekov[46], M. Dreval[46], C. Dritselis[47], S. Dubbioso[18], L. Dubus[3], R. Ducker[8], H. Dudding[8], R. Dumont[3], P. Dumortier[33], D. Dunai[19], M. Dunne[6], A. Durif[3], G. Durr-Legoupil-Nicoud[8], B. Duval[8], R. Dux[6], F. Ebrahimi[48], L. Edes[8], A. Ekedahl[3], S. Elmore[7], E. Emanuelli[49], G. Ericsson[17],

[*] Author to whom any correspondence should be addressed.

F. Eriksson[7], J. Eriksson[17], B. Eriksson[17], D. Ernst[50], B. Esposito[16], E. Fable[6], M. Faitsch[6], D. Fajardo[6], N. Fakhrayi Mofrad[11], G.L. Falchetto[3], A. Fanni[23], N. Fedorczak[3], J. Ferreira[41], N. Ferron[1], L. Fevre[3], O. Fevrier[8], O. Ficker[9], A. Field[7], L. Figini[14], A. Figueiredo[41], P. Figueiredo[30], A. Fil[3], F. Fiorenza[18], D. Fiorucci[16], M. Firdaouss[3], R. Fischer[6], M. Fitzgerald[7], J. Flanagan[7], L. Fleury[3], T. Fonghetti[3], J.M. Fontdecaba Climent[24], P. Forestier-Colleoni[3], A. Frank[8], E. Fransson[51], L. Frassinetti[52], D. Frattolillo[18], D. Frigione[1], S.L. Fugazza[20], S. Futatani[39], S. Gabriellini[7,53], G. Galatola Teka[16], K. Galazka[37], J. Galdon-Quiroga[22], S. Galeani[35], D. Gallart[54], A. Gallo[3], C. Galperti[8], M. Gambrioli[1], S. Garavaglia[14], S. Garcia Herreros[8], M. Garcia Munoz[22], J.L. Gardarein[51], L. Garzotti[7], J. Gaspar[51], R. Gatto[53], P. Gaudio[35], E. Gauthier[3], M. Gelfusa[35], J. Gerardin[3], S. Gerasimov[7], G. Gervasini[14], E. Geulin[3], Z. Ghani[7], F.M. Ghezzi[14], L. Gil[41], A. Gillgren[31], E. Giovannozzi[16], C. Giroud[7], T. Gleiter[6], M. Gobbin[1,2], V. Goloborodko[55], J. Gonzalez-Martin[22], G. Gorini[20], D. Gossard[27], M. Grandin[1], G. Granucci[38], G. Grassler[10], G. Grenfell[6], M. Griener[6], W. Gromelski[37], M. Groth[11], O. Grover[6], M. Gruca[37], N. Grzybicka[37], A. Gude[6], C. Guillemaut[3], A. Guillevic[31], S. Guinchard[8], R. Guirlet[3], J. Gunn[3], T. Gyergyek[42], L. Hagg[17], P. Halldestam[6], C. Ham[7], D. Hamm[8], J. Harrison[7], E. Hasan-Toneva[56], N. Hawkes[7], S. Hegedus[19], P. Heinrich[6], C. Heiß[8], S. Henderson[7], P. Hennequin[57], C. Hernandez[3], J. Hillairet[3], A. Hjalmarsson[17], J. Hobirk[6], E. Hodille[3], R. Hojlund[40], M. Hölzl[6], M. Hoppe[52], J. Horacek[9], N. Horsten[34], A. Houben[26], J. Hromadka[9], Q. Hu[20], J. Hua[26], Z. Huang[7], A. Huart[3], A. Hubbard[50], A. Huber[26], P. Huynh[3], M. Iafrati[16], V. Igochine[6], F. Imbeaux[3], P. Innocente[1,2], N. Isernia[18], H. Isliker[58], V. Ivanov[9], P. Ivanova[56], I. Ivanova Stanik[37], S. Jachmich[59], P. Jacquet[7], M. Jagielski[37], L. Jansen[30], A. Jansen van Vuuren[8], A. Jardin[37], A. Jardin[60], H. Järleblad[40], A. Järvinen[5], F. Jaulmes[9], I. Jepu[7], M. Jimenez Comez[22], D. Jordan[5], J. Bryant[7], D. Kabirov[22], S. Kachkanov[7], J. Kalis[6], A. Kallenbach[6], J. Karhunen[5], A.N. Karpushov[8], E. Kaselouris[45], S. Kasilov[10], Y. Kazakov[33], P.V. Kazantzidis[13], H.T. Kim[7], D. King[7], V. Kiptily[7], A. Kirjasuo[5], A. Kirk[7], K. Kirov[7], A. Kirschner[26], A. Kit[5], T. Kiviniemi[11], A. Knieps[26], S. Kobussen[30], G. Kocsis[19], L. Kogan[7], J. Kolsen de Wit[40], Y. Kominis[13], M. Komm[9], M. Kong[8], B. Kool[30], S.B. Korsholm[40], D. Kos[7], M. Koubiti[51], J. Kovačič[42], Y. Kovtun[46], E. Kowalska-Strzeciwilk[37], K. Krieger[6], D. Kropackova[9], O. Krutkin[8], I. Kudashev[51], O. Kudlacek[6], H. Kuivasniemi[11], Y. Kulyk[46], U. Kumar[8], H. Kumpulainen[26], R. Kwiatkowski[61], M. La Matina[1], M. Ladygina[37], A. Lafay[52], L. Laguardia[14], P. Lainer[10], V. Laporta[14], M.R. Larsen[40], K. Lawson[7], M.Y.K. Lee[8], N. Lemoine[32], F. Lengyel[19], M. Lennholm[7], C. Leoni[53], E. Lerche[33], N. Leuthold[62], X. Li[6], Y.C. Liang[6], Y. Liang[26], J. Likonen[5], K. Lim[8], X. Litaudon[3], E. Litherland-Smith[7], G. Lo-Cascio[6], T. Loarer[3], L. Lobko[9], B. Lomanowski[44], J. Lombardo[1], N. Lonigro[7,63], R. Lorenzini[1], T. Lunt[6], J. Macdonald[7], R. Mackenbach[8], E. Macusova[9], R. Mäenpää[11], P. Maget[3], C. Maggi[7], S. Malec[9], J. Malinak[9], K. Malinowski[37], P. Manas[3], D. Mancini[8], P. Mantica[14], M. Mantsinen[54,64], M. Maraschek[6], G. Marcer[20], C. Marchetto[65], S. Marchioni[8], A. Mariani[14], M. Marin[8], D. Maris[30], M. Markl[10], T. Markovic[9], L. Marrelli[1,2], C. Martin[28], S. Masillo[8], M. Maslov[7], R. Masocco[35], V. Masson[8], M. Mattei[18], S. Mattogno[35], D. Matveev[26], M.L. Mayoral[7], D. Mazon[3], D. Mazur[66], S. Mazzi[3], K. McKay[22], A. Andrew[7], A. Mele[8], V. Menkovski[25], S. Menmuir[7], J. Merchand[39], A. Merle[8], K. Mikszuta-Michalik[37], D. Milanesio[49], L. Milia[23], I.G. Miron[43], R. Mirowski[61], S. Misdanitis[67], R. Mishra[37], J. Mitchell[7], R. Mitteau[3], V. Mitterauer[6], D. Moiraf[3], V. Moiseenko[46], P. Molina[8], S. Molisani[1,2], F. Mombelli[12], I. Monakhov[7], C. Monti[16], A. Montisci[23], J. Morales[3], D. Morbey[7], A. Moreau[6], P. Moreau[3], R. Morgan[8], J. Moritz[32], A. Moro[14], D. Moulton[7], A. Murari[1,2], A. Muraro[14], K. Murray[7], O. Myatra[7], D. Mykytchuk[8], F. Nabais[41], Y. Nakeva[21], F. Napoli[16], M.F. Nave[41], A. Nelson[62], A.H. Nielsen[40], S.K. Nielsen[40], A. Niemelä[5], M. Nocente[20], R. Nouailletas[3], S. Nowak[14], H. Nyström[52], M. O'Mullane[7], R. Ochoukov[6], S. Olasz[19], C. Olde[7], J. Oliver[7], J. Ongena[33], J.M. Ordonez Jimenez[22], A. Orduna Martinez[6], L. Orlandi[1], C. Orrico[30], F.P. Orsitto[16], R. Osawa[7], A. Osipov[31], R. Otin[7],

J.J. Palacios Roman[30], D.I. Palade[43], O. Pan[6], N. Panadero[24], A. Panera Alvarez[30], P. Papagiannis[13], G. Papp[6], V. Parail[7], A. Parrott[7], K. Paschalidis[68], M. Passoni[12], F. Pastore[8], B. Patel[7], A. Patel[7], A.H. Patel[6], A. Pau[8], E. Pawelec[66], M. Pedrini[8], G. Pelka[37], E. Peluso[16,35], A. Perek[8], J. Gonzalez-Martin[22], J. Perez Gonzalez[22], C. Perez Von Thun[37], F. Pesamosca[59], M. Peterka[9], K. Petersen[40], P. Petersson[52], L. Pigatto[1], L. Piron[1], C. Piron[1,16], A. Pironti[18], F. Pisano[23], V. Plyusnin[41], M. Podesta[8], A. Podolnik[9], Y. Poels[8], G. Pokol[19], J. Poley[8], L.M. Pomarjanschi[43], M. Poradzinski[7,37], L. Porte[8], C. Possieri[35], I. Predebon[1,2], G. Pucella[16], F. Puentes del Pozo[22], M.J. Pueschel[25], P. Puglia[3], T. Pütterich[6], V. Quadri[3], M. Rabinski[61], R. Ragona[40], M. Rasinski[26], J. Rasmussen[40], G. Ratta[24], S. Ratynskaia[68], T. Ravensbergen[59], M. Rebai[14], D. Rees[11], D. Refy[19], M. Regine[35], H. Reimerdes[8], M. Reisner[6], B. Reman[40], P. Ren[26], C. Reux[3], A. Reyner-Vinolas[22], D. Ricci[14], M. Richou[3], S. Rienäcker[57], D. Rigamonti[14], F. Rigollet[51], V.P. Rikala[11], F. Rimini[7], N. Rispoli[14], N. Rivals[3], A. Rodriguez Gonzalez[22], J.F. Rivero-Rodriguez[7,22], T. Rizzi[68], C. Roach[7], M.M. Robaldo[49], S. Rode[26], P. Rodrigues[41], V. Rohde[6], J. Romazanov[26], R. Rossi[35], G. Rubino[14], J. Rueda-Rueda[69], F. Ruffini[1], P. Ryan[7], D. Ryan[7], J. Rzadkiewicz[61], S. Saarelma[7], S. Saari[5], R. Sabot[3], M. Sackers[26], D. Sales de Oliveira[8], M. Salewski[40], A. Salmi[5], C. Salvia[1], L. Sanchis[22], J. Santos[41], S. Sartorello[1], O. Sauter[8], R. Scannell[7], J. Schatzlmayr[10], L. Schiesko[3], B.S. Schmidt[69], P.A. Schneider[6], N. Schoonheere[3], K. Schutjes[30], L. Scotti[20], F. Scotti[70], J. Seidl[9], L. Senni[71], G. Sergienko[26], S. Setzu[23], D. Sgrelli[3], S. Sharapov[7], R. Sharma[7], U. Sheikh[8], G. Sias[23], B. Sieglin[6], S. Silburn[7], C. Silva[41], A. Silva[41], D. Silvagni[6], L. Simons[8], J. Simpson[7], L. Singh[49], S. Sipilä[11], M.M. Skyllas[31], E.R. Solano[24], M. Sos[9], C. Sozzi[14], S. Spagnolo[1,2], C. Srinivasan[7], A. Stagni[1], Z. Štancar[7], G. Stankunas[72], D. Stieglitz[6], J.Stobbs[6,73], P. Strand[31], F. Subba[49], H. Sun[7], G.Y. Sun[8], H. Sun[8], W. Suttrop[6], J.P. Svantner[8], J. Svoboda[9], D. Svorc[9], G. Szepesi[7], T. Szepesi[19], F. Taccogna[14], R. Takacs[6], T. Tala[5], P. Tamain[3], M. Tan[26], W. Tang[6], M. Tardocchi[14], D. Taylor[7], G. Telesca[37], A. Tenaglia[35], D. Terranova[1,2], D. Testa[8], C. Theiler[8], E. Tholerus[7], B. Thomas[7], A. Thrysoe[40], Q. Tichit[3], A. Titarenko[46], P. Tolias[68], E. Tomasina[1], M. Tomes[9], A. Tonel[1], E. Tonello[8], A. Tookey[7], B. Tosto[20], E. Trier[7], J.W. Tumbokon[8], M. Tunkl[9], A. Uccello[14], M. Ugoletti[1,2], P. Ulbl[6], G. Urbanczyk[32], A. Valentini[40], M. Valovic[7], M. van Berkel[25,30], D. Van Eester[33], G. Van Parys[8], M. van Rossem[8], B. Vanovac[50], H.P. Varadarajan[30], S. Vartanian[3], M. Vavrik[19], M. Vaz[41], J. Vega[24], L. Velarde Gallardo[22], C. Venturini[8], M. Veranda[1,2], T. Verdier[40], G. Verdoolaege[15], K. Verhaegh[7,25], L. Vermare[74], A. Vesa[11], J. Vicente[41], E. Viezzer[22], L. Vignitchouk[68], F. Villone[18], C. Vincent[7], B. Vincent[8], P. Vincenzi[1,2], J. Vinklárek[9], P. Virtanen[11], I. Voitsekhovitch[7], L. Votta[52], M. Vulcano[35], T. Vuoriheimo[75], E. Wang[26], Y. Wang[8], C. Wang[8], Y. Wang[73], T. Wauters[59], H. Weisen[8,76], N. Wendler[37], A. Widdowson[7], S. Wiesen[30], M. Wiesenberger[40], T. Wijkamp[30], M. Willensdorfer[6], M. Winkel[25], A. Wojenski[77], E. Wolfrum[6], H. Wu[15], I. Wyss[35], Q. Xia[7], L. Xiang[7], P. Xie[26], S. Xu[26], D. Yadykin[31], X. Yan[26], Y. Yang[26], H. Yang[51], K. Ye[26], R. Zagorski[61], P. Zanca[1], K.D. Zastrow[7], Y. Zayachuk[7], J. Zebrowski[61], P. Zenz[10], M. Zerbini[16], P. Zestanakis[13], H. Zhang[6], Y. Zhang[15], W. Zholobenko[6], B. Zimmermann[6], A. Zito[6], M. Zlobinski[26], V.K. Zotta[53], M. Zuin[1,2] and M. Zurita[8]

[1] Consorzio RFX (CNR, ENEA, INFN, University of Padova, Acciaierie Venete SpA), C.so Stati Uniti 4, 35127 Padova, Italy
[2] Istituto per la Scienza e la Tecnologia dei Plasmi, CNR, Padova, Italy
[3] CEA, IRFM, F-13108 Saint-Paul-lez-Durance, France
[4] Nuclear Department, ENEA, Frascati, Italy
[5] VTT Technical Research Centre of Finland, PO Box 1000, FIN-02044 VTT, Finland
[6] Max-Planck-Institut für Plasmaphysik, D-85748 Garching, Germany
[7] United Kingdom Atomic Energy Authority, Culham Campus, Abingdon, Oxon OX14 3DB, United Kingdom of Great Britain and Northern Ireland

[8] École Polytechnique Fédérale de Lausanne (EPFL), Swiss Plasma Center (SPC), CH-1015 Lausanne, Switzerland
[9] Institute of Plasma Physics of the CAS, Za Slovankou 1782/3, 182 00 Praha 8, Czech Republic
[10] Graz University of Technology, Petersgasse 16, 8010 Graz, Austria
[11] Aalto University, PO Box 14100, FIN-00076 Aalto, Finland
[12] Politecnico di Milano, Milan, Italy
[13] National Technical University of Athens, Iroon Polytechniou 9, 157 80 Zografou, Athens, Greece
[14] Institute for Plasma Science and Technology, CNR, via R. Cozzi 53, 20125 Milano, Italy
[15] Department of Applied Physics, Ghent University, 9000 Ghent, Belgium
[16] ENEA, NUC, Centro Ricerche Frascati, Via E. Fermi 45, 00044 Frascati (Roma), Italy
[17] Department of Physics and Astronomy, Uppsala University, Uppsala SE-75120, Sweden
[18] Consorzio CREATE, Via Claudio 21, 80125 Napoli, Italy
[19] Centre for Energy Research, POB 49, H-1525 Budapest, Hungary
[20] University of Milano-Bicocca, Piazza della Scienza 3, 20126 Milano, Italy
[21] DEIM Department, Universitá degli Studi della Tuscia, Viterbo, Italy
[22] Universidad de Sevilla, Sevilla, Spain
[23] Department of Electrical and Electronic Engineering, University of Cagliari, Piazza d'Armi, 09123 Cagliari, Italy
[24] Laboratorio Nacional de Fusión, CIEMAT, Madrid, Spain
[25] Eindhoven University of Technology, Eindhoven, Netherlands
[26] Forschungszentrum Jülich GmbH, Institute of Fusion Energy and Nuclear Waste Management-Plasma Physics, 52425 Jülich, Germany
[27] Ecole Supérieure d'Ingénieurs Léonard de Vinci (ESILV), De Vinci Higher Education, De Vinci Research Center, 92 916 Paris, France
[28] Aix-Marseille University, CNRS, PIIM, UMR 7345 Marseille, France
[29] Laboratoire J.A. Dieudonné, Université Cote d'Azur, UMR 7351, Parc Valrose, 06108 Nice cedex 2, France
[30] Dutch Institute for Fundamental Energy Research, PO Box 6336, 5600 HH Eindhoven, Netherlands
[31] Chalmers University of Technology, SE-41296 Gothenburg, Sweden
[32] Institut Jean Lamour, CNRS-Université de Lorraine, UMR 7198, 54500 Vandoeuvre-lés-Nancy, France
[33] Laboratory for Plasma Physics,LPP-ERM/KMS, B1000 Brussels, Belgium
[34] Department of Mechanical Engineering, KU Leuven, Leuven, Belgium
[35] Universitá di Roma Tor Vergata, Via del Politecnico 1, Roma, Italy
[36] General Atomics, San Diego, CA, United States of America
[37] Institute of Plasma Physics and Laser Microfusion, Hery 23, 01-497 Warsaw, Poland
[38] DTT ENEA C. R. Frascati, via E. Fermi 45, 00044 Frascati (Roma), Italy
[39] Universitat Politécnica de Catalunya, Barcelona, Spain
[40] Department of Physics, Technical University of Denmark, Bldg 309, DK-2800 Kgs Lyngby, Denmark
[41] Instituto de Plasmas e Fusão Nuclear, Instituto Superior Técnico, Universidade de Lisboa, 1049-001 Lisboa, Portugal
[42] Faculty of Mechanical Engineering, Jožef Stefan Institute, Ljubljana, Slovenia-University of Ljubljana, Ljubljana, Slovenia
[43] The National Institute for Laser, Plasma and Radiation Physics, Magurele-Bucharest, Romania
[44] Oak Ridge National Laboratory (ORNL), UT Battelle for the U.S. Department of Energy,1 Bethel Valley Road, Oak Ridge, TN 37830, United States of America
[45] Hellenic Mediterranean University, Institute of Plasma Physics and Lasers, Tria Monastiria, Rethymnon Crete T.K. 74100, Greece
[46] National Science Center 'Kharkov Institute of Physics and Technology', Akademichna 1, Kharkiv 61108, Ukraine
[47] Department of Civil Engineering, University of Thessaly, Pedion Areos, 38334 Volos, Greece
[48] Princeton Plasma Physics Laboratory, Princeton, NJ, United States of America
[49] Politecnico di Torino, Corso Duca degli Abruzzi 24, 10129 Torino, Italy
[50] Plasma Science and Fusion Center, Massachusetts Institute of Technology, Cambridge, MA, United States of America
[51] Aix-Marseille University, CNRS, IUSTI, UMR 7343, 13013 Marseille, France
[52] Electromagnetic Engineering and Fusion Science, KTH Royal Institute of Technology, SE-100 44 Stockholm, Sweden
[53] Dipartimento di Ingegneria Astronautica, Elettrica ed Energetica, SAPIENZA Universitá di Roma, Via Eudossiana 18, 00184 Roma, Italy
[54] Barcelona Supercomputing Center, Barcelona, Spain
[55] Institute for Nuclear Research, Prospekt Nauky 47, Kyiv 03680, Ukraine
[56] Institute of Electronics, Bulgarian Academy of Sciences (BAS), 72 Tsarigradsko Chaussee, Sofia, 1784, Bulgaria

[57] Laboratoire de Physique des Plasmas (LPP), CNRS, Sorbonne Université, École polytechnique, Institut Polytechnique de Paris, Palaiseau, France
[58] section of Astrophysics, Astronomy and Mechanics, Physics Department, Aristotle University, Thessaloniki, GR 541 24, Greece
[59] ITER Organization, Route de Vinon-sur-Verdon-CS 90 046, 13067 St Paul Lez Durance Cedex, France
[60] Institute of Nuclear Physics Polish Academy of Sciences (IFJ PAN), Radzikowskiego 152, 31-342 Krakow, Poland
[61] National Centre for Nuclear Research (NCBJ), 05-400 Otwock-Świerk, Poland
[62] Dept Appl Phys & Appl Math, Columbia Univ, New York, NY 10027, United States of America
[63] Department of Physics, York Plasma Institute, University of York, York YO10 5DD, United Kingdom of Great Britain and Northern Ireland
[64] ICREA (Catalan Institution for Research and Advanced Studies), Barcelona, Spain
[65] Dipartimento Energetica, CNR, Institute for Complex Systems, and Politecnico di Torino, Corso Duca degli Abruzzi 24, Torino, 10129, Italy
[66] Institute of Physics, University of Opole, Oleska 48, 45-052 Opole, Poland
[67] Department of Mechanical Engineering, University of Thessaly, Pedion Areos, 38334 Volos, Greece
[68] Space and Plasma Physics, KTH Royal Institute of Technology, Stockholm, SE-100 44, Sweden
[69] Department of Physics and Astronomy, University of California, Irvine, CA 92697, United States of America
[70] Lawrence Livermore National laboratory, Livermore, CA, United States of America
[71] Institute for Applied Mathematics, CNR, via dei Taurini 19, 00185 Rome, Italy
[72] Laboratory of Nuclear Installation Safety, Lithuanian Energy Institute, Breslaujos Str. 3, LT-44403 Kaunas, Lithuania
[73] Aalborg University, Pontoppidanstræde 111, 1.009, 9220 Aalborg Øst, Denmark
[74] Laboratoire des Physique des Plasmas (LPP), Ecole polytechnique, Palaiseau, France
[75] University of Helsinki, PO Box 43, Helsinki FI-00014, Finland
[76] V.N. Karazin Kharkiv National University, Kharkiv, Ukraine
[77] Warsaw University of Technology, Nowowiejska 15/19, 00-665 Warsaw, Poland

E-mail: nicola.vianello@igi.cnr.it

Received 24 December 2025, revised 21 April 2026
Accepted for publication 22 May 2026
Published 22 June 2026

Abstract

JET, the only tokamak capable of operating with deuterium–tritium (D–T) fuel (since TFTR was shutdown in 1999), has provided essential experimental data to support ITER and DEMO design and operation. Within the EUROfusion Tokamak Exploitation Work Package, JET completed its final campaigns (2022–2023), culminating in the third D–T campaign (DTE3). These experiments addressed key challenges in plasma scenarios, exhaust control, and tritium management under reactor-relevant conditions. Significant progress was achieved in demonstrating ITER-like integrated scenarios with impurity seeding, achieving partial divertor detachment and high confinement ($H_{98}(y,2) \approx 0.85$) at 3 MA in D–T plasmas. Advanced exhaust regimes such as quasi-continuous exhaust (QCE) and *X*-point radiator (XPR) were successfully achieved first in D–D and then extended to D–T operation, confirming their relevance for mixed isotope operation. Operational milestones included a new world record of 69 MJ fusion energy in tritium-rich hybrid plasmas and long-pulse H-mode operation up to 60 s, contributing with unique data to the CICLOP database. Physics studies focused on peeling-limited pedestals in support of ITER and improved understanding of edge stability and impurity screening in metallic environments. Extensive usage of the shattered pellet injector (SPI) on JET provided critical information for the design of the ITER disruption mitigation system (DMS). Real-time control systems for D/T ratio control and plasma exhaust were deployed and demonstrated in D–D and D–T, while energetic particle physics investigations unfolded the role of fast ions in turbulence suppression mechanisms. Comprehensive tritium retention studies using gas balance method, post-mortem analysis, and ITER-relevant laser induced desorption spectroscopy (LIDS) diagnostics provided essential input for tritium accountancy strategies. These results are validating the ITER operational concepts, inform DEMO design, and deliver critical experience in nuclear operation and scenario integration.

Keywords: magnetic fusion, D–T, plasma scenarios, plasma-wall interaction, disruptions, runaway electrons, control

(Some figures may appear in colour only in the online journal)

1. Introduction

To ensure safe operation margins in next-step fusion devices such as ITER and future power plants, experiments on large tokamaks using deuterium–tritium (D–T) fuel mixtures are essential to test scenarios scaling capabilities and compatibility with mixed isotope operation. These studies provide critical data for understanding plasma physics under conditions approaching those of burning plasmas, while also informing operational procedures and identifying technological challenges. JET has played a pivotal role in this context for over 40 years [1], being the only device, together with TFTR, capable of operating with D–T mixtures. Designed as a large tokamak to explore reactor-relevant plasma behaviour, JET was engineered to confine a significant fraction of alpha particles, up to 90% at 2.5 MA [2]. Following the first D–T campaign (DTE1, 1997) [3], which revealed unacceptable tritium retention [4], JET transitioned in 2010 from carbon to all-metal plasma-facing components (PFCs) (beryllium main chamber, tungsten divertor) [5] , pioneering metallic wall operation in large tokamaks [2]. In 2021, JET conducted its second D–T campaign (DTE2) [6], achieving major milestones: a record fusion energy output of 59 MJ, improved confinement and reduced energy losses in D–T plasmas compared to pure deuterium, and enhanced understanding of energetic ion dynamics and multiscale transport [6, 7]. These results strengthened confidence in predictive modelling and provided new insights into isotope effects, plasma-wall interactions (PWI), and RF heating–all essential for ITER's D–T operation. From 2022 to 2023, JET scientific program was integrated into the EUROfusion Work Package Tokamak Exploitation (WPTE) [8], alongside ASDEX Upgrade, MAST-U, TCV, and WEST. This coordinated effort leveraged the unique capabilities of each device to address key physics questions for ITER and DEMO. This activity culminated with the final JET DT campaigns, DTE3 [9], and the outcomes of this campaign as well as the rest of the DD operation in 2022-2023 are presented in this overview.

Leveraging the capabilities of individual devices, the WPTE program aims to strengthen confidence in scenario extrapolation, key physics understanding, and technical solutions for next step fusion devices. It adopts a stepladder approach from mid-size tokamaks to JET, enabling exploration of a broader parameter space in terms of size, plasma current, heating mix and power, shaping, and PFCs. JET's contribution has been essential for validating physics models and scenario scalability to larger devices in a metallic environment with higher heating power and isotope mixtures thanks to its T handling capabilities. The JET experimental program under WPTE spanned about two years (2022–2023) and came after a campaign in Helium, previously reported in [10]. Figure 1 illustrates the sequence of campaigns presented in this contribution designed as a single program where D–T operations extended the preceding deuterium campaigns [8, 9]. The inclusion of the JET device into this multi-machine program was guided by a set of high-level objectives exploiting the unique JET capabilities to complete and expand the plasma physics knowledge and therefore progress along the research pillars of WPTE program as described in [8]. These high levels objectives can be summarized as follow:

Validate scenarios for next step devices: with exploration in D and D–T to confirm compatibility in mixed-isotope species. Several scenarios were considered for the campaign, each of them pursued in view of potential solution for future larger device. This included the ITER-relevant baseline H-mode with extrinsic impurity seeding to ensure effective exhaust handling; the no-ELM/small-ELMs scenarios and in particular the *quasi continuous exhaust* (QCE) [11]; the highly radiative *X*-point radiator scenarios (XPR) [12] and high-β_N operation in view of potential application to JT-60SA, as well as scenarios developed initially for the DTE2 campaign like the high-current baseline [13].

Addressing key physics gaps: towards next step devices. Among the key topics identified for metallic devices effort was devoted to the pedestal transport and stability at low ν^* [14], further experimental investigation of high-*Z* impurities screening [15] and further understanding of the role of fast ions in turbulence stabilization and MHD activity.

Secure the safe and reliable operation for next step devices: this scientific pillar was pursued via the full exploitation of the JET Shattered Pellet Injection to inform ITER disruption and runaway electron (RE) mitigation strategies, the advancement of integrated plasma control compatible with D–T operation and the increase of knowledge of deuterium and tritium retention

From the organizational point of view the last JET operation period tried to maximize the machine time availability, properly weighting the operational risks with the awareness of being the last chance of exploring issues that only JET could address. The transition from Deuterium to D–T operation was determined on the basis of a specific set of milestones conceived to guarantee:

1. The completion of key scientific objectives in D–D before D–T transition
2. The thorough preparation and the demonstration of readiness of main target scenarios for D–T operation
3. The completion of the shattered pellet injector (SPI) program, essential to inform ITER disruption mitigation system (DMS) design, knowing that the SPI had to be disconnected from the vessel before D–T operation without the possibility to reinstall it before the JET final shutdown.

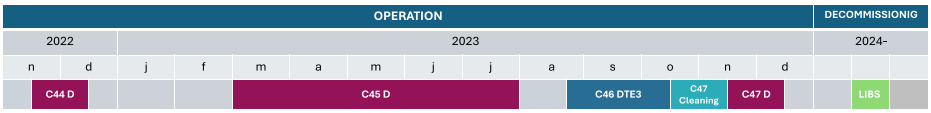

Figure 1. JET timeline for the period described in the present contribution started in November 2022. The violet colour indicates operation in Deuterium, dark blue colour the DTE3 operation, light blue the cleaning operation. The JET operation ended on the 18th of December 2023 and started the corresponding decommissioning activities. LIBS exploitation, during non-campaign operation was performed in August 2024.

The procedure put in place allowed to maximize the scientific outcome of the campaign within the tight operational constraints linked to the end-of-life of JET.

DTE3 operation strongly benefited from the recent DTE2 campaign, enabling the optimization of operational procedures thanks to the recent experience in operating with mixed isotopes and properly documented in [16]. Unlike DTE2, both neutral beam boxes in DTE3 were operated in deuterium, offering higher reliability than tritium beams and minimizing the change over time. Operations were organised in sessions rather than single pulses. This offered higher flexibility to the organisation of the programme thus providing the possibility to adapt the programme of the session according to the results obtained as well as to the machine daily technical condition. As before, the campaign was constrained by the JET lifetime neutron budget limit of 2×10^{21} 14 MeV neutrons. DTE2 and DTE3 together accounted for 86.8% of this budget [9], thus confirming the optimal usage of the machine capabilities. Operation immediately after the end of DTE3 were planned to clean the residual tritium amount in the vessel and ensure a safe decommissioning at the end of 2023. As detailed in section 4.3, the cleaning procedure targetted a value of $\lesssim 1\%$ of T gas in the plasma and the reduction of tritium content in the exhaust gas below 0.02%: once reached JET entered its final Deuterium campaign, as indicated in figure 1, aimed to collect appropriate Deuterium reference to pulses executed in DTE3 and extend operation to to unexplored boundaries as for the case of the long-pulse operation described in section 2.6 or negative triangularity.

In the first section, this paper will address the development of scenarios compatible with a metallic wall. Exhaust solutions for steady heat loads (such as detachment control) and transient heat loads (such as ELMs) are discussed. Novel scenarios developed in smaller devices like the QCE or the XPR regime have been successfully implemented on JET and in addition run in both D–D and D–T. The next section will present the physics issues relevant for next step devices, namely the physics conditions for achieving impurity screening, the exploration of pedestal collisionality and stability in conditions close to ITER and the fast ion physics in D–T plasma including alpha particles. Finally, the paper will show important items essential for the safe operation of ITER and the future fusion power plant. This includes the mitigation of disruptions and run-aways, the reliable control of detachment isotope ratio in D–T and the inventory and recovery the fuel using novel diagnostics relevant for the fusion power plant.

2. Scenario validation for next step devices

2.1. JET-ITER baseline scenario with Ne seeding

In its reference 15 MA baseline scenario, ITER is expected to operate with a partially detached divertor (with outer target temperature $T_e \lesssim 5$ eV), achieved through a combination of high divertor neutral pressure and extrinsic impurity seeding [17], whilst maintaining a hot pedestal and high core performance. These core-edge integration studies have been one of the main programmatic line since the installation of the JET-ILW [18].

To support the ITER operational point and provide a robust dataset for model validation and scenario extrapolation, the Ne-seeded JET-ITER baseline scenario has been developed in the last deuterium campaigns and in DTE3. This scenario has been designed with a magnetic configuration close to the ITER foreseen one, with a closed divertor configuration and both the strike points hitting the divertor vertical targets while feathering an high triangularity ($\delta_u = 0.33$–0.40, $\delta_l = 0.35$)shape. This scenario leverages on earlier experiments at 2.5 MA/2.7 T in deuterium campaign preceding DTE2 operation [19], which demonstrated the feasibility of Ne-seeded plasmas with good performance ($H_{98y2} \approx 0.9$) and high radiation fraction ($f_{rad} \approx 0.86$) under high-recycling divertor conditions: these conditions were sustained for 4 s without W accumulation and without significant ELM activity [19]. In DTE2, it was possible to re-establish the key features of this scenario: a similar rise in the energy confinement time and normalised pressure, improved pedestal pressure and the transition to small ELMs with the increase in Ne concentration. Partial detachment was obtained but the confinement remained modest in DTE2 with an input power limited to 23–25 MW instead of the anticipated 28–30 MW.

Motivated by these promising results, dedicated experiments were conducted in 2022–2023 to expand the operational space and investigate core-edge-exhaust integration. Studies covered both deuterium and deuterium–tritium plasmas at higher input power, higher plasma current, and lower pedestal collisionality. The goal was to understand conditions for Type-I ELM-free plasmas with Ne and N seeding (the latter in D only). Discharges operated at high input power (30–35 MW) with plasma current from 2.5 MA to 3.2 MA, and q_{95} from 2.7 to 3.3.

In the D–D campaign prior to DTE3, high-performance Ne-seeded plasmas with $I_p = 2.5$ MA, $B_t = 2.7$ T and P_{in} up to 37 MW (with a combination of NBI and ICRH heating)

demonstrate the robustness of the scenario as well as the reliable and reproducible access to ELM-free conditions. The scenario features a good confinement (up to $H_{98}(y,2) \approx 0.9$) considering that it was obtained with high radiation fraction $f_{\rm rad} \approx 70\%$ and partial detachment of the outer strike point (OSP) with Ne seeding. It is worth mentioning that, in agreement with what earlier presented [19], for this specific scenario the radiation fraction estimated has been corrected to achieve power balance following the methodology available in [20].

The pedestal is substantially modified with increased Neon content, with a reduction of pedestal density and a simultaneous increase of both ion and electron temperature (reaching pedestal electron temperature $T_{\rm e,ped} \approx 1$ keV and pedestal ion temperature $T_{\rm i,ped} \approx 1.5$ keV to 2 keV for pedestal Neon concentration $C_{\rm Ne} = 1.5\%$–2%) leading to a pedestal collisionality of $\nu^*_{\rm e,ped} \approx 0.3$–$0.5$.

While the overall pedestal pressure increases, its gradient becomes shallower. The confinement improvement with increasing Neon content is primarily attributed to the enhanced pedestal temperature, with secondary contributions from an increased $E \times B$ shear (rotation) and additional benefit from improved core turbulence stabilization due to ion dilution [21–23].

The ELM activity is substantially modified by the increased Neon content with no collapse of the pedestal, reaching conditions without distinct ELM activity as monitored by infrared target temperature for $C_{\rm Ne} = 1.5\%$ (with D-gas rate between 3.5–4.5×10^{22} el s^{-1}). Both ideal and resistive MHD stability analysis were performed [24, 25]: the reduction of the pedestal gradient with Neon is found together with a widening of the pedestal width. Resistive MHD description proved to describe ELM triggering both in unseeded and seeded case [25]. Attempts to extend the scenario to higher current up to 3.2 MA were technically challenging. The goal was to further reduce the pedestal top collisionality and test the scenario for lower scrape off layer heat flux width λ_q. However, the narrow operational window in terms of available power with respect to *L–H* transition posed significant constraints. Additionally, the risk of large electromagnetic (EM) forces in case of disruption was a concern. Even at maximum available power ($P_{\rm in} \approx 37$ MW), plasmas at 3.2 MA/3.45 T could not be sustained in stable H-mode. Only modest performance was achieved at 3.0 MA/2.9 T ($H_{98y2} \approx 0.7$), as shown in the right panel of figure 2.

Operation in D–T further expanded the accessible parameter space, likely due to beneficial isotope effects reducing the LH power threshold [26]. This is shown in the right panel of figure 2 where D–D and D–T plasmas at 3.0 MA/2.9 T with equivalent engineering parameters are shown highlighting clear better confinement properties obtained with mixed isotope operation. In the left panel of the same figure 2, a similar comparison is shown for 2.5 MA/2.7 T where similar confinement properties in D–D and D–T could be obtained.

D–T operation enabled the demonstration of a fully integrated Ne-seeded scenario at 3 MA/2.9 T with partial divertor detachment ($P_{\rm in} \approx 34$ MW, $f_{\rm GW} \approx 0.75$, $\beta_N \approx 2$, $H_{98y2} \approx 0.85$), sustained for more than 7 s without tungsten accumulation and no significant ELM-activity as observed from the infrared target temperature. Example of this scenario with the best achieved performances are reported in [9] (figure 1) as well in figure 10. This scenario provides a unique dataset on core-edge integration and an integrated team of specialists is working together to understand the complex picture of interconnected phenomena (such as pedestal transport and stability, near and far SOL transport and improved confinement with Neon) combining efforts from global gyrokinetic simulations, 2D fluid codes, and integrated reduced models to understand this scenario with the aim of increasing the reliability of predictions for ITER.

2.2. Implementation of small or no-ELM scenarios on JET: the QCE regime

While the ITER baseline assumes operation with RMP-suppressed ELMy scenarios, DEMO-class devices will require robust small-ELM or no-ELM regimes to avoid unacceptable transient heat loads from ELM filaments. These operational modes must also ensure adequate particles and impurities exhaust to prevent core plasma contamination and performance degradation. The QCE is a natural Type-I ELM free regime which has emerged as a promising candidate for such applications [27, 28], featuring high core and edge density which could facilitate impurity and helium ash exhaust while maintaining good confinement and pedestal performance. The QCE regime is characterized by the presence of small, frequent filamentary like activity that provide continuous particle and heat exhaust, thereby reducing peak divertor heat loads and keeping pedestal pressure away from the large scale peeling-ballooning stability limit.

The access condition to QCE for JET was established by leveraging experience gained in medium size tokamaks like ASDEX-Upgrade [28, 29] and TCV [30]; requirements include strong plasma shaping quantified by the shaping parameter $S_{\rm d} = \kappa^{2.2}(1+\delta)^{0.9}$-and high separatrix density [29], the former providing stabilizing mechanisms for global peeling-ballooning pedestal modes, whereas the latter ensuring the destabilization of local ballooning modes, at the bottom of the pedestal, which create benign transport before global instabilities develop. This initial understanding enabled the determination of an operational space for establishing the QCE on JET which nevertheless required careful operation, to cope with additional heat load on the upper dump plate not conceived to handle high heat flux [31]. The QCE scenario has been established with current up to $I_{\rm P} = 2.25$ MA with strong plasma shaping ($S_{\rm d} > 5$) and high separatrix density. This was achieved with high triangularity ($\delta_{\rm up} \approx 0.47$) and elongation ($\kappa \approx 1.83$), closely matching ITER projections [11, 32]. High fuelling rates were employed, ensuring separatrix electron temperatures $T_{\rm e,sep} \approx 110 - 130$ eV and densities of $n_{\rm e,sep} \approx 1.5 - 3.5 \times 10^{19}$ m^{-3}. Once the QCE scenario was established, residual activity is observed in divertor spectroscopy signals (such as Be II, W-I line emission, or Infrared maximum temperature). These fluctuations are interpreted as filaments expelling plasma from the confined region without affecting the pedestal top values as indicated by the absence

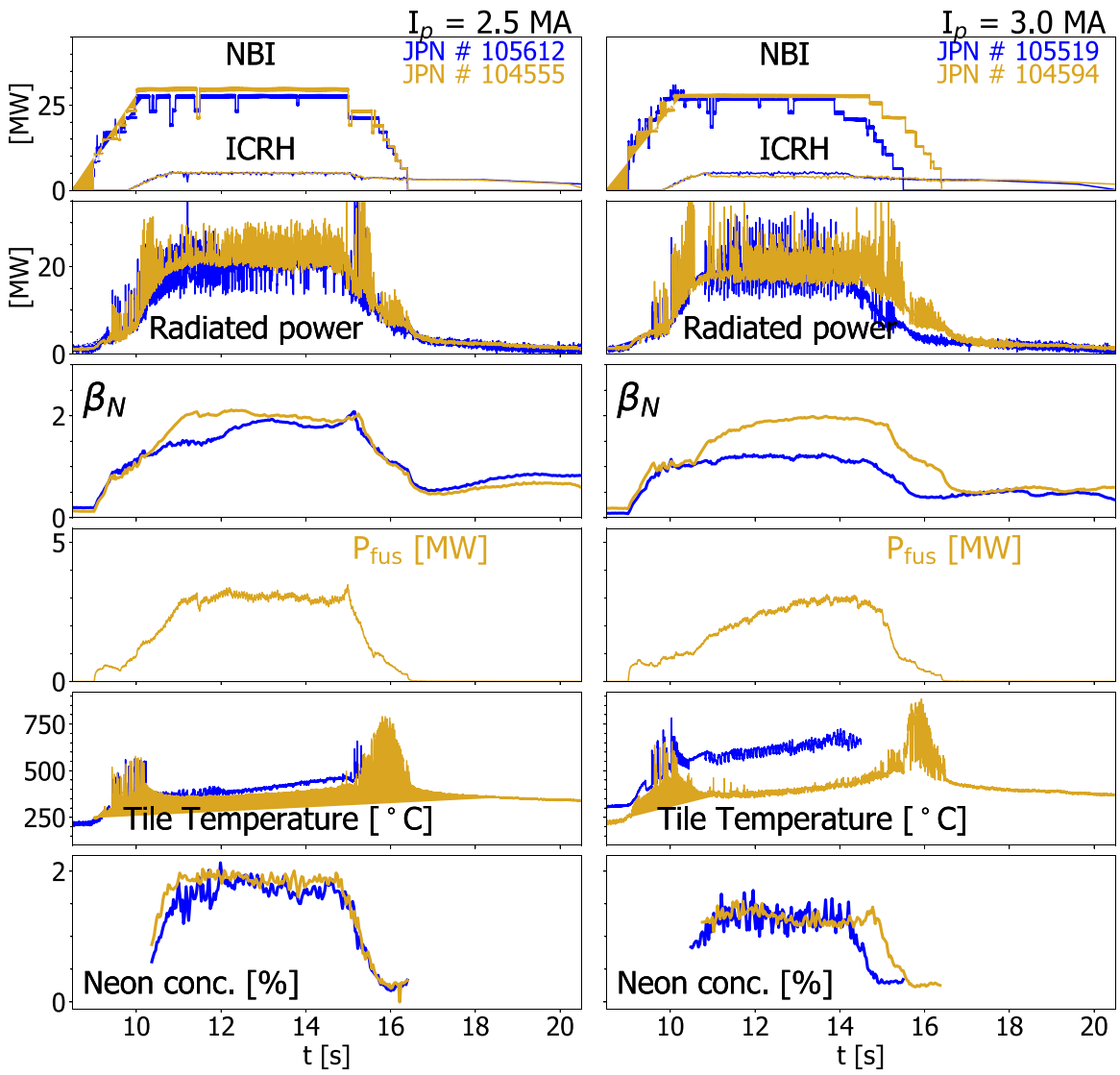

Figure 2. Left column: Time traces comparison for shots 105612 and 104555, both at 2.5MA/2.7 T and respectively in D–D and D–T. From top to bottom: input power, radiated power, normalized pressure β_N, Fusion power (for the D–T case), outer divertor target maximum temperature from infrared measurement, Neon concentration in the pedestal region. The right column present a similar comparison for two shots at 3.0 MA, 105519 (blue) and 104 600 (gold), respectively in D–D and D–T. It can be clearly seen that in the D–D case the plasma remains in L-mode without significant improvement in β_N during the high power phase.

of fluctuations in ECE channels at the top of the pedestal. This confirms the achievement of a Type-I ELM free scenario, although further work is underway to address the role of these filaments on power load and tungsten sputtering both from the target and first wall plasma facing components. An example of a discharges where shape modification allowed to move from Type-I ELMy regime to QCE is shown in figure 3. In particular the time evolution of shaping parameter S_d is shown together with the time traces of maximum temperature at the target and pedestal temperature as estimated by an ECE channel close to pedestal top. The figure clearly shows how moving the plasma to the QCE increased shape produces the vanishing of ELM signature, both at the target and at the pedestal top, thus showing the sensitivity of small-ELM regime to plasma shape. Moderate neon seeding further aided in reducing divertor heat flux and improving operational flexibility: the amount of extrinsic impurity employed resulted in core concentrations of $c_{Ne} \approx 0.8\%$. This seeding increased radiated power from 5.8 MW to 10.5 MW and decreased peak divertor temperature variations ΔT from 130 K s^{-1} to 40 K s^{-1}, approaching partial detachment, albeit without reducing particle flux. Operation on JET expanded the parameter space explored in medium size tokamaks also in term of achievable pedestal top collisionality which reached values as low as $\nu^*_{e,ped} \approx 0.9$ [11]. A database of steady-state QCE phases (> 400 ms) was established, covering plasma currents from 1.5 to 2.25 MA, toroidal fields from 2.3 to 3.3 T, heating powers from 11 to 31 MW, normalized pressures β_N from 1.0 to 2.4, pedestal densities from 0.50 to 0.75 f_{GW}, pedestal collisionalities ν^*_e from 0.9 to 2.0, and radiated fractions f_{rad} from 0.2 to 0.6 [32], extending therefore the parameter space explored in medium size tokamaks.

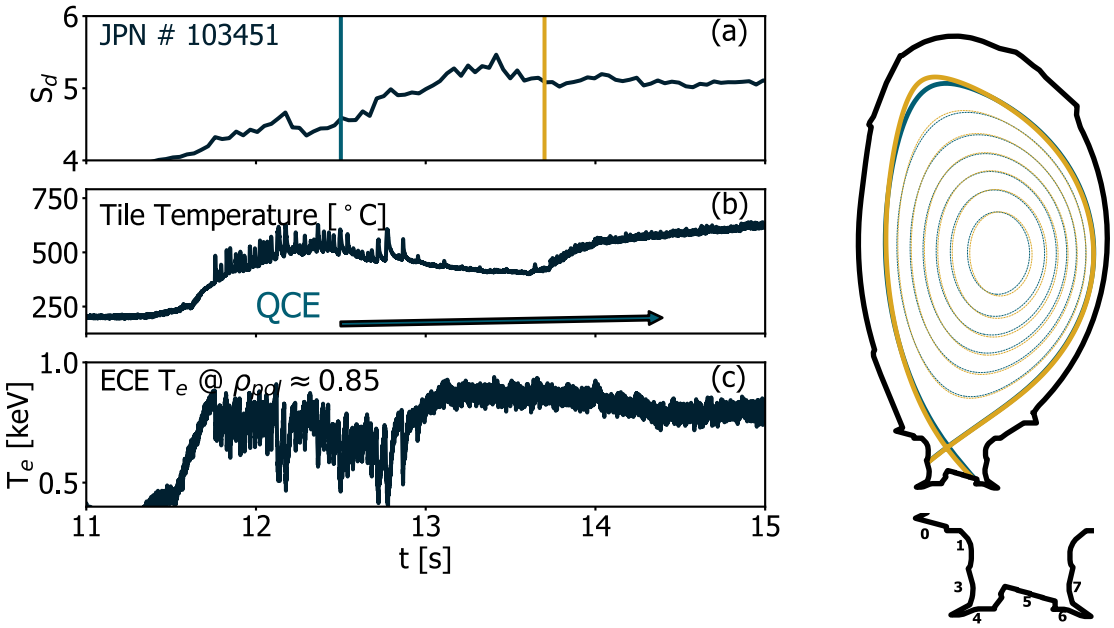

Figure 3. Example of transition from Type-I ELMy regime to QCE regime on JET D–D discharge. From top to bottom: (*a*) time evolution of shaping parameter S_d (*b*))time trace of maximum target temperature as measured by infrared thermography; (*c*) ECE radiometer channel close to pedestal top. Both (*b*) and (*c*) are showing the disappearance of ELM signature at the top of pedestal when moving to the QCE high shaping magnetic configuration. In the panel on the right plasma shapes at time instants indicated by vertical lines in panel (*a*) are shown exhibiting the changes when moving from Type-I ELMy to QCE-like space. The insight provides a zoom on divertor geometry where divertor tile numbers are shown for reference. Reproduced from [32]. The Author(s). CC BY 4.0.

The QCE regime was successfully demonstrated in D–T plasmas during the DTE3 campaign, confirming its compatibility with mixed isotope operation. Comparative analysis of matched D–D and D–T pulses showed similar filament characteristics and ELM suppression at identical shaping and fuelling conditions. Pedestal profiles revealed higher electron and ion temperatures, as well as higher pedestal density in D–T, resulting in increased plasma pressure at comparable heating power [32]. Since the QCE is a high density regime, only moderate central temperature was achievable on JET, therefore limiting the fusion power achievable. High absolute densities are expected for accessing QCE regime in ITER and DEMO, albeit at significantly higher pedestal temperatures than those achievable in present-day machines. Future predictions of fusion power in the QCE regime should be developed in comparison with what is expected for the baseline ELMy H-mode scenario. Nevertheless, the successful demonstration of the QCE in D–T plasmas is an important milestone for this regime, since no-significant show-stopper arose in mixed isotope operation, making this operational mode a viable candidate for future devices requiring no-ELM regimes including ITER [29, 33].

2.3. XPR Regime

Protecting divertor PFCs from extreme heat and particle flux is critical for reactor operation, where DEMO-class devices are expected to operate at high dissipative fractions ($f_{rad} \approx 95\%$), exceeding ITER's target. In this respect, the XPR regime is a promising solution for power exhaust in fusion power plant relevant conditions, achieving the requested radiation fraction ($f_{rad} \gtrsim 70\%$) and potential ELM reduction while maintaining a relatively good confinement. A stable solution of a localized region near or slightly above the *X*-point, characterized by intense radiation, low electron temperature (1–2 eV) and high plasma density has been experimentally identified and reproducible achieved in all the major devices including ASDEX-Upgrade and JET [12]. On JET initial operation with XPR regime was achieved at modest power [34, 35] with feed-forward extrinsic impurities only. Extensive work in medium size tokamaks confirmed, an XPR stable solution can be controlled in real-time (RT) by carefully monitoring the XPR vertical position thus providing a powerful system for detachment control [36]. During the D–D campaign preceding DTE3 JET achieved stable XPR scenarios using heating powers up to 26 MW in low triangularity ($\delta = 0.22$) H-mode plasmas (I_p =2.5 MA, B_t =2.7 T). The XPR was explored initially by single impurity seeding testing different species such as Nitrogen, Neon, or Argon. While Nitrogen was discarded, given its incompatibility with D–T operation due to potential tritiated-ammonia production [37], pure Neon or Argon seeding led to persistent L–H dithering, attributed to excessive core radiation (Argon) or unfavourable pedestal transport (Neon) at this plasma shape and power. Stable operation was achieved using mixed Ar–Ne seeding, avoiding dithering across a broad range of Ar/Ne ratios. In these conditions, the divertor remained fully detached, and the radiated power fraction, not corrected for achieving power balance, reached up to 75% [38]. ELM activity diminished progressively with increasing XPR height and vanished near the vertical position

corresponding to the highest location which could be properly controlled before disruption. No substantial degradation of plasma performances was observed whenever transitioning from ELMy to no-ELM regime in XPR regime. The XPR scenario exploration strongly benefitted from an extensive work on RT control of detachment and [36, 39]. The control deployed on JET was based on sensors and actuators compatible with D–T operation. The XPR position was tracked using the KB5H bolometer system, with a spatial resolution enabling continuous monitoring. Control was implemented via RT controlled Argon injection, while Neon was programmed in feed-forward. The controller gains were optimized using system identification techniques [36], allowing robust performance despite actuator delays of approximately 1 s caused by the long gas lines and injection valve dynamics. The control achieved positional accuracy within about 4 mm above the *X*-point and operated effectively across mixed and pure Argon seeding phases: it demonstrated robustness with respect to programmed power variations or transient events as pellet injection. This capability enabled dynamic impurity ratio scans while maintaining stable power exhaust. Despite the fact that XPR on JET was previously achieved as well with feed-forward only impurity seeding [34], the RT control provided a significant improvement in stability and operational flexibility, allowing the exploration of a wider parameter range, limiting the disruption risk and ensuring a safe transition to XPR no-ELM space and longer steady-state phases.

The XPR regime and its control were successfully deployed in D–T plasmas during JET's DTE3 campaign. Noteworthy is that the RT control of the XPR position worked smoothly when transferred from D–D to D–T plasma, exhibiting the same detachment dynamics and proving an easy transfer from different isotope mixtures. In D–T discharges, the XPR was maintained at a safe vertical position, far from potential position causing plasma disruption (experienced from precedent D–D experiments), while transitioning from mixed Ar–Ne to pure Ar seeding. Figure 4 compares seeded and unseeded D–T pulses: seeded cases achieved $f_{\mathrm{rad}} \geqslant 70\%$ (not corrected for power balance), modestly increased stored energy and confinement, and importantly showed no significant pedestal degradation in no-ELM conditions. Investigation on kinetic profiles, also shown in figure 4, indicate that the energy gain is mainly attributed to the increase in core electron density, with minor T_{e} contribution [12]. Detailed modelling of the XPR regime in D–T plasmas is ongoing to elucidate impurity transport and radiation distribution, as well as to assess core-edge integration aspects. The successful demonstration of the XPR regime in D–T plasmas with RT control marks a significant advancement towards robust power exhaust solutions for future fusion reactors. Thanks also to the successfull demonstration of the XPR in D–T plasma, the scenario is now also considered as a potential candidate for ITER, where modelling activities are in progress to test the compatibility with divertor design as well as potential impact on confinement [40].

2.4. JET baseline scenarios

Since the installation of the ITER-like wall (ILW), the JET baseline scenario has been developed for high-current operation with tungsten. Initial scenario development showed reduced performance and confinement in ILW compared to JET-C wall [41]. However, the high performance previously obtained with the JET-C wall was ultimately matched in ILW after four years of development and optimization [42]. This achievement required establishing an operational balance between two competing requirements: the lowest feasible gas dosing necessary to access high-performance regimes, and the amount of gas needed to sustain sufficient ELM activity required for edge density and W control. The fuelling strategy that ultimately enabled this consisted of low gas puffing combined with 2 mm pacing pellets for ELM triggering.

The JET baseline scenario development [13] has been carried out through a stepwise increase of plasma current in D plasmas, from 2.5 MA up to 4 MA. This progressive approach inspired the ITER re-baselining strategy [43], which foresees alternating D–D and D–T operation during the current increase towards the target value. Already during scenario development in D, the challenges of operating at high current $I_{\mathrm{p}} \geqslant 3.5$ MA became evident: access to the high-performance regime required the full availability of all tokamak systems (high auxiliary heating, pellet injection, low impurity concentration, etc) and was further constrained by low-q_{95} operation ($q_{95} \sim 2.8$) imposed by toroidal field limits. In addition, since auxiliary heating on JET is limited ($P_{\mathrm{aux}} = 40$ MW nominally foreseen for DTE2 [42] with $P_{\mathrm{aux}} = 34$ MW actually achieved [6]), operational point was ultimately set at (3.5 MA / 3.3 T). This was chosen as a compromise to reduce the risk of disruption at high current operation.

In DTE2, plasma performance aligned with extrapolations from D–D to a 50–50 D–T mixture [44], but D–T plasmas systematically exhibited higher pedestal-top density and weaker ELM activity [45]. The reduction in ELM frequency consistently led to tungsten accumulation in the low-field side (LFS), resulting in early pulse termination via the protection systems triggered on high radiated fraction. Therefore, while the JET baseline scenario could be routinely sustained for the full 5 s flat-top duration in D–D at 3.5 MA, transferring it to full T and D–T conditions reduced sustained pulse duration to only ∼2–3s. Extensive investigations were performed to clarify the role of impurity transport [46, 47] and the influence of experimental conditions, starting from core–pedestal transport studies [48] to fully integrated COCONUT core-edge-SOL modelling [49]. COCONUT results indicate a reduced pedestal fuelling efficiency in T with respect to D plasmas when operating at low particle throughput: this has severe impact on the ELM activity, with the disappearing of the benign compound ELM activity observed in D–D [45] when moving to D–T, and thence an increased impurity content observed experimentally.

In DTE3, the scenario was revisited to understand why it could not be sustained at a plasma current of 3.5 MA. Operation at high current above 3.5 MA were nevertheless

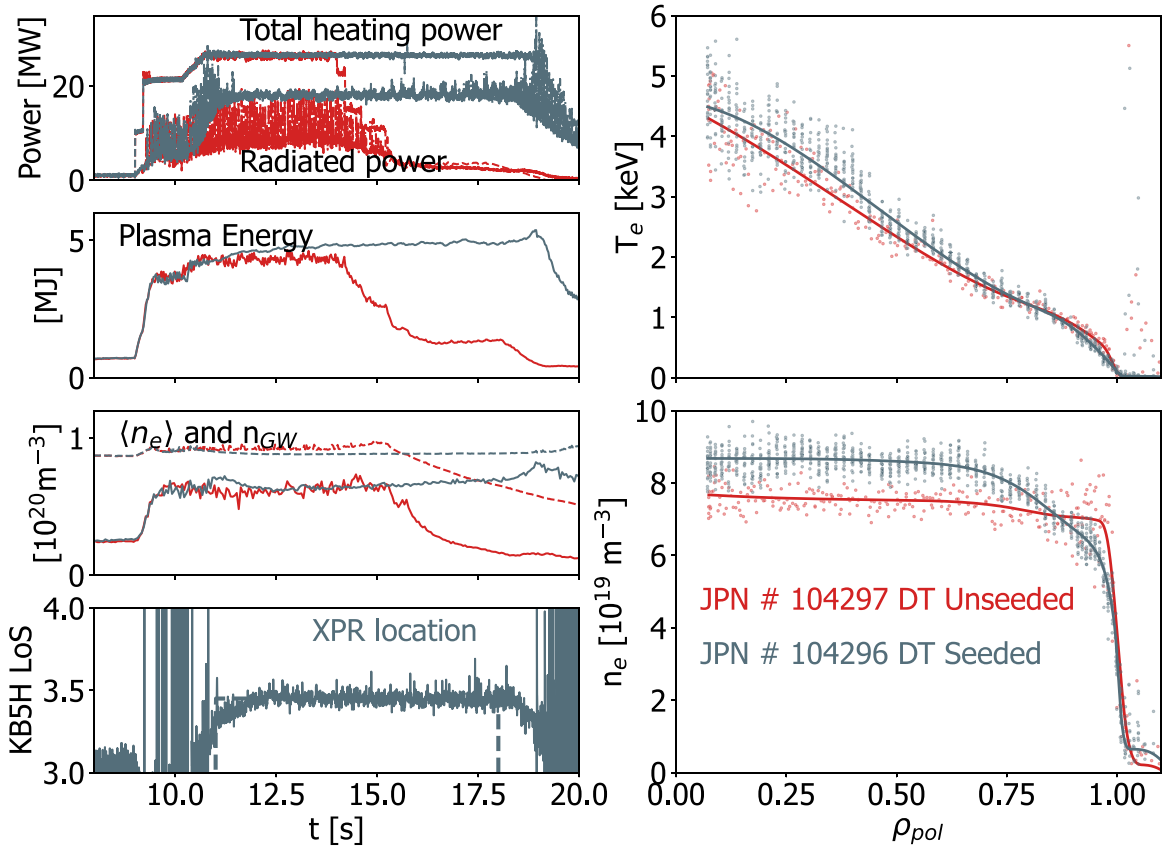

Figure 4. Comparison of a seeded and unseeded XPR discharge in DT plasmas. On the left from top to bottom: total heating power and radiated power, Plasma stored energy, line average density (solid) and corresponding Greenwald density (dashed), real time detection of XPR. On the right: top panel Temperature profiles, bottom panel density profiles. Both the shots were operated at 2.65 T/2.5MA. Reproduced from [12]. CC BY 4.0.

avoided, as they were posing severe machine risk which could potentially compromised PFCs samples intended for post-mortem analysis. The main operational difference relative to DTE2 was the use of pure-D NBI in DTE3. To account for this, the fuelling scheme was re-evaluated via integrated modelling [50], starting from the (3.0 MA/2.8 T) DTE2 reference pulse and successfully adapted to achieve a 50–50 D–T mixture in experiments. However, D-NBI fuelling caused a radial T-concentration gradient, producing a D-rich core and 50–50 (or slightly T-rich) edge plasmas [51]. Since thermal neutron fraction in baseline pulses typically exceeds 60% (i.e. $f_n > 0.6$), core D-enrichment degraded the fusion performance. First attempts in DTE3 at (3.0 MA/2.9 T) with increased tritium fuelling reproduced higher frequency ELM activity as seen in DTE2 (JPN # 104661, see figure 5(*a*)). With a further increase in the gas fuelling rate (JPN # 104662, figure 5(*b*)), the MHD activity limited the performance and the plasma stability when maximum heating power was applied. This was mitigated by slightly reducing the input power ($P_{\mathrm{NBI}} \approx 27$ MW, $P_{\mathrm{RF}} \approx 3$ MW), enabling—for the first time—a JET-ILW baseline pulse in D–T sustained for more than 5 s (pulse JPN 104663) until programmed termination ((∼ 7 s before increasing gas to allow discharge soft landing)).

The extensive JET high-current D–T database carries strong relevance for ITER, providing insights into isotope effects, pellet fuelling, high-current operational limits, and W-induced radiation asymmetries. However a key operational lesson concerns the difficulty of transferring a scenario optimised in D directly to D–T, in particular whenever operating in condition where potential disruptions could cause severe damages as was the case for high current. Even a well-established D reference may lack critical components when applied to D–T conditions. Future devices—including ITER—should therefore aim to minimize the risk associated to the scenario development in D, while allocating a sufficient time to further develop the plasma scenarios in D–T to establish the region of optimal performance and robustness of the scenario itself and potentially increase our confidence and capability to .predict the transition from D–D to D–T.

2.5. *High-β scenario investigation in support of JT-60SA*

With JT-60SA approaching its operational phase under the Broader Approach agreement, a dedicated experimental campaign was carried out on JET-ILW to provide a reference dataset for future high-β scenarios on JT-60SA. The experimental design is grounded in the dimensionless similarity principle [52]: two non-burning tokamak plasmas are confinement-equivalent when they share the same

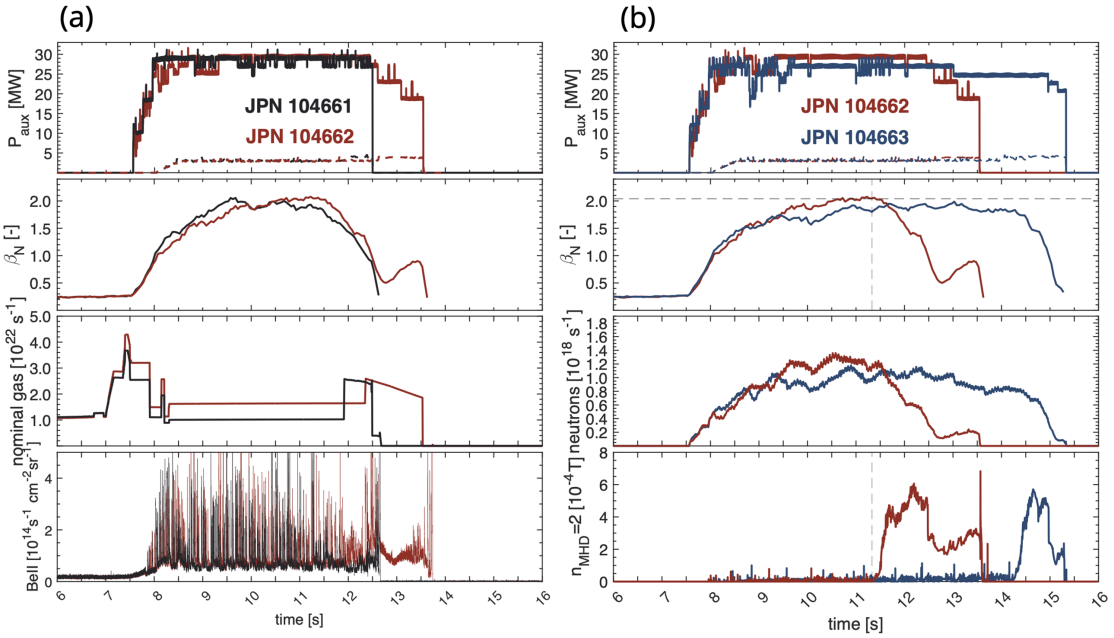

Figure 5. JET baseline scenario development during DTE3 at 3.0 MA / 2.9 T. Pulse 104661 exhibits weakened ELM activity similar to that observed in DTE2. Increasing the gas fuelling in pulse 104662 leads to an extension of the pulse duration, but an $n = 2$ MHD mode is triggered likely due to a β_N limit (indicated by the dashed line in the second panel of plot (*b*)). A reduction of the additional heating power in pulse 104663 mitigates the MHD activity, allowing the pulse duration to be further extended up to the pre-programmed termination. In the top panels of (*a*) and (*b*) NBI and ICRH powers are respectively indicate in solid and dashed lines.

values of the normalised Larmor radius $\rho^* = \rho_i/a$, normalized collisionality $\nu^* \propto n_e q R T_e^{-2} \varepsilon^{3/2}$, normalised pressure $\beta = \langle p \rangle / (B^2/2\mu_0)$, and safety factor profile q, together with the same magnetic geometry. In these definitions ρ_i is the ion Larmor radius, a the plasma minor radius, $\varepsilon = a/R$ the inverse aspect ratio, $\langle p \rangle$ the volume-averaged plasma pressure, and B the on-axis magnetic field [52]. For plasmas with equal major radius and ion mass, enforcing this equality yields engineering parameter scaling as a function of the aspect-ratio scalings $B \propto A^{15/8}$ and $I_p \propto A^{-1/8}$ [52]. Applied to JET ($A = 3.2$) and JT-60SA ($A = 2.7$), which share $R \approx 3$ m, these give $B_{JET}/B_{SA} \approx 1.37$ and $I_{p,JET}/I_{p,SA} \approx 1.02$, so that JET discharges at $(B_T, I_p) = (2.4\ \mathrm{T}, 1.4\ \mathrm{MA})$ are dimensionlessly similar to JT-60SA discharges at $(1.7\ \mathrm{T}, 1.4\ \mathrm{MA})$. The weak aspect-ratio dependence of $\beta_{N,max} \approx A^{-1/2}$ [53] further implies that the MHD equilibrium properties at high β will be closely matched between the two devices.

Guided by these constraints deuterium plasmas, hereafter referred to as the JET/JT-60SA experiments [54], were produced in a variant of the hybrid-advanced scenario with the following parameters: $B_T = 1.7$, 2.0, and 2.4 T; $I_p = 1.4$ MA; elongation $\kappa = 1.6$–1.7; triangularity $\delta \approx 0.4$–0.45; $q_{95} = 4$–6; central safety factor $q_0 > 1.1$ at NBI onset; $P_{NBI} = 13$–25 MW; no ICRH. Discharges at $B_T = 2.4$ T were executed during DTE3. The high-triangularity configuration was chosen for its beneficial effects on pedestal confinement and MHD stability. The dataset extends the 2014 hybrid power scan at high δ as reported in [55] by broadening the NBI power range from 15 to 25 MW at $B_T = 1.7$ T, and by operating at $q_{95} > 5$ relative to the 2014 advanced-scenario pulses [56] at $B_T = 2.4$ T. Systematically, NBI power scans ($P_{NBI} = 13$–25 MW) were performed at three values of q_{95} (4, 5, and 6) at fixed shape ($\delta = 0.45$, $\kappa = 1.7$) and at low-to-moderate gas injection rates ($< 1 \times 10^{22}$ es). Two complementary scans were conducted: (i) a NBI power scan modulating β_N; and (ii) a NBI onset-time scan controlling q_0 at the start of the main heating phase, which is a key parameter for MHD stability of the high-β phase.

The degree of dimensionless similarity achieved is illustrated in figure 6, which compares the dimensionless parameters of the JET/JT-60SA discharges with the JT-60SA design values for the scenarios identified as IV-2 and V-2 on the JT-60SA Research Plan [57] and with JET high-triangularity discharges at the same toroidal field from [58] (cfr figure 3 on the mentioned publication). The JET/JT-60SA experimental discharges are seen to occupy the same region of dimensionless parameter space as the JT-60SA reference scenarios, validating the applicability of the similarity approach. In these discharges on JET, poloidal Larmor radius $\rho_P^* = 0.036$ and bootstrap current fraction $f_{BS} = 0.6$ were obtained, matching the corresponding JT-60SA target values, consistent with global confinement being primarily governed by ρ^* [52].

The dependence of the maximum normalized beta on NBI input power, shown in figure 7, provides further characterization of the confinement regime exhibiting a quasi-linear dependence of β_N on P_{NBI}. The main experimental results are as follows. Reliable control of the q_0 at the onset of the main heating phase was demonstrated, with the optimal NBI start time $t_{0,NBI}$ exhibiting the expected dependence on toroidal magnetic field B_T, consistent with the behaviour observed in earlier JET hybrid and advanced scenarios. Good confinement properties were achieved with β_N increasing with input

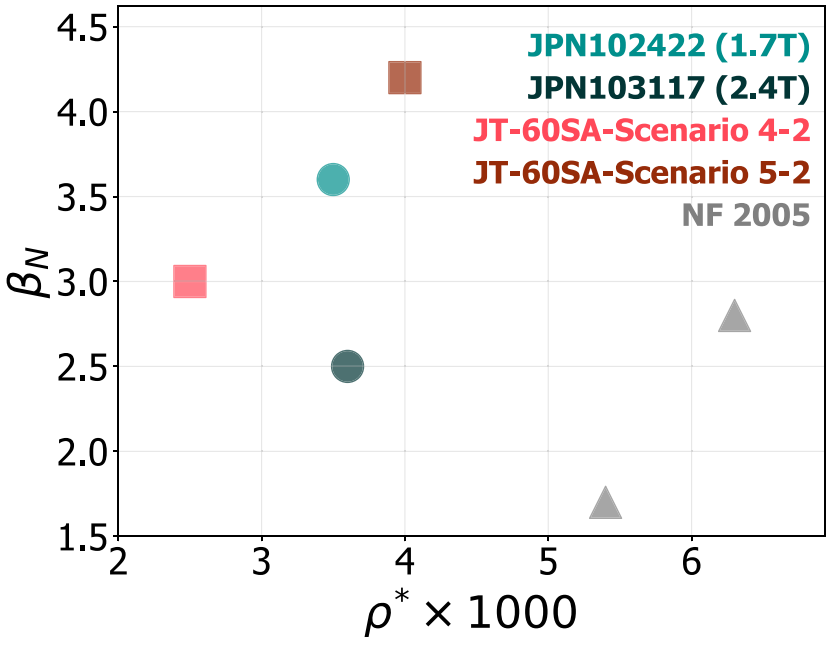

Figure 6. Comparison of dimensionless plasma parameters for JT-60SA design scenarios (squares) as available from JT-60SA Research Plan [57] , JET/JT-60SA experimental discharges (circles), and JET hybrid-scenario discharges from [58] (triangles).

power and reaching $\beta_N \approx 3.7$–4.0 at $B_T/I_p = 1.7$ T/1.4 MA and $\beta_N \approx 2.9$–3.2 at $B_T/I_p = 2.4$ T/1.4 MA, with relatively mild and stable MHD activity in the hybrid-advanced configuration. Taken together, these results demonstrate the feasibility of realizing discharges on JET-ILW that are dimensionlessly similar to the JT-60SA reference scenarios, providing a validated experimental basis for predicting confinement and MHD stability properties of future JT-60SA operation.

2.6. Long pulse operation and new fusion energy record

During the final JET-ILW campaign, long-duration deuterium discharges were performed to assess plasma sustainment over multiple resistive times and study plasma–wall interactions in a full-metal environment [59]. These experiments required major technical adjustments across subsystems, including plasma shape control, machine protection, and diagnostics [60]. They achieved the highest injected energy in JET with the ILW ($E_{in} = 450$ MJ), pushing the limits of the inertially cooled divertor and auxiliary heating systems. The results are now contributing to the multi-machine CICLOP (coordination on international challenges on long duration operation) database [61] and supported ITER-relevant developments. Figure 8 shows time traces of a 60 s H-mode discharge (JPN # 105750, $B_0 = 1.9$ T, $I_p = 1.4$ MA) with 4 to +6 MW NBI and 2 MW ICRH for the first 36 s. The strike point was shifted from vertical divertor plate (Tile 7, see inset of figure 3 for tile numbering layout) to the horizontal one (Tile 6) to comply with the divertor energy handling capabilities of JET-ILW; tile 6 phase delivered $E_{in} = 323$ MJ, slightly above the tile limit (315 MJ), thus requiring special authorization. The stored energy remained in the range of $\approx 1.6 - 1.8$ MJ with electron and ion temperature $T_{e0} \approx T_{i0} \approx 3.0 - 3.5$ keV during combined heating. After ICRH stopped (due to its limited pulse length to 40 s), T_e dropped but stored energy remained constant due to higher density and lower radiation. Energy confinement was constant during the entire discharge at approximately $\tau_E \approx 0.25 - 0.3$ s). Bulk radiation was low during the horizontal tile phase (Tile 6), with no impurity accumulation observed despite a transient event at $t = 34$ s. Type-I ELMs (50–70 HZ) persisted throughout. Earlier vertical tile (Tile 7) operation showed higher radiation and marginal impurity control due to intermittent ELMs near the L–H power threshold. The discharge consumed ∼80% of the available ohmic flux and could have been extended by about 25 s with sustained auxiliary heating [60], with the duration determined only by engineering constraints and no physical limits. JET-ILW long pulses extended the CICLOP database, which benchmarks long-pulse performance for future reactors. Figure 9 plots the triple product $n_i \cdot \tau_E \cdot T_i$ versus high-performance duration for multiple devices. JET-ILW points (red diamonds) stand out, maintaining $n_i \cdot \tau_E \cdot T_i \approx 0.05 - 0.06$ atm. s with minimal degradation up to 60 s–about five times higher than comparable-duration entries in the 2024 CICLOP dataset. Note on this figure that $n_i \cdot \tau_E \cdot T_i = 0.7$ corresponds approximately to Q = 1. Since these results (Dec 2023), other devices have extended their records; updates has been recently presented [62].

Despite DTE3 not being focused on the achievement of high fusion performance, nevertheless time was dedicated to further refine and improve the T-rich beam target scenarios which provided the highest fusion energy output during DTE2 [63]. The scenario is conceived to maximize the D_{fast}-T reaction in a T rich plasma, where the population of fast Deuterons is coming primarily from the NBI system. While

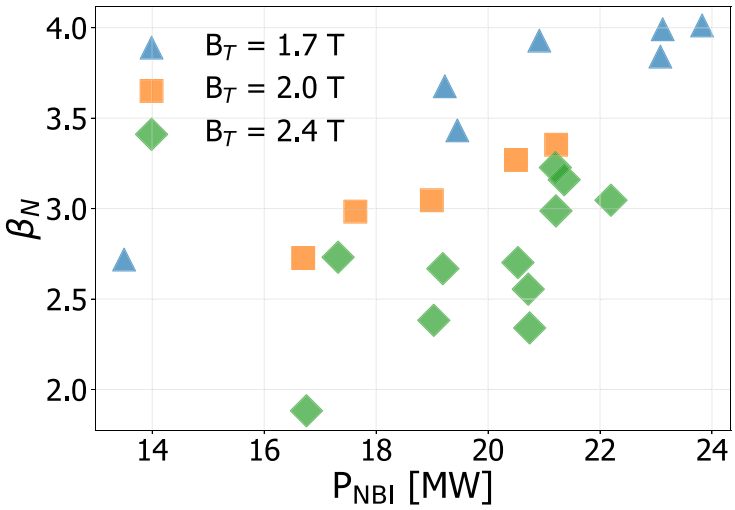

Figure 7. Maximum normalized beta β_N as a function of NBI heating power P_{NBI} (MW) for different toroidal magnetic fields.

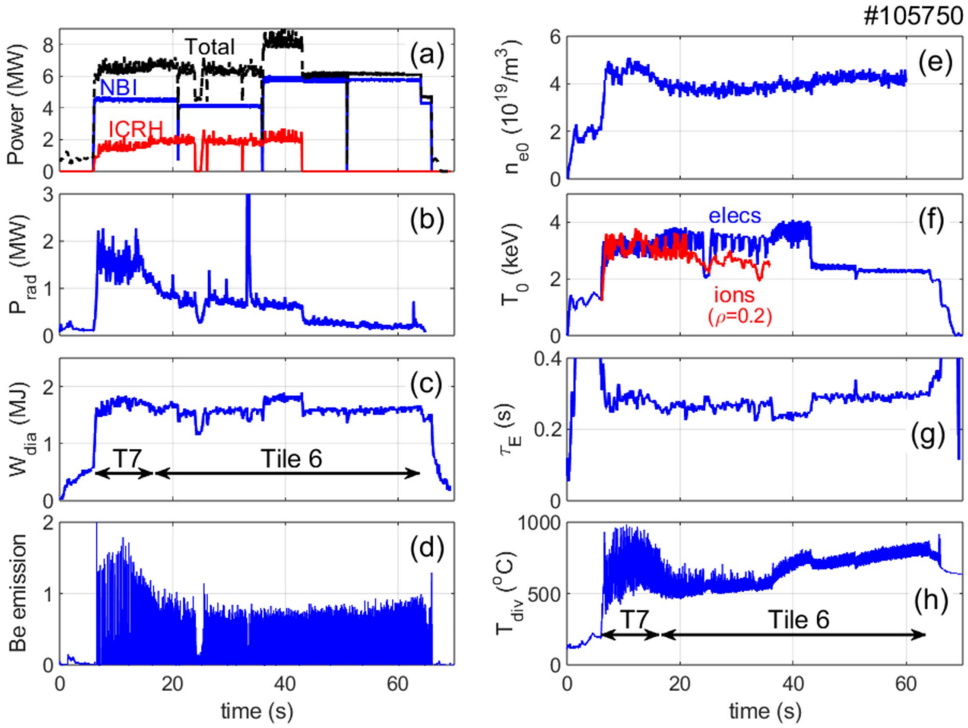

Figure 8. (*a*) Time traces of a 60 s H-mode discharge (JPN 105750, $B_0 = 1.9$ T, $I_p = 1.4$ MA) with 4–6 MW NBI and 2 MWICRH for the first 36 s. (*a*) NBI and ICRH power, (*b*) Bulk radiated power from bolometer, (*c*) Internal stored energy, (*d*) Be-I emission line (*e*) Central electron density from High Resolution Thomson Scattering (HRTS) and (*f*) Central ion and electron temperature from Charge Exchange Recombination Spectroscopy (CXRS) and ECE respectively. (*g*) Energy confinement time (*h*) Divertor temperature from IR camera. Reproduced from [59]. © The Author(s). Published by IOP Publishing Ltd CC BY 4.0.

such a scenario is not directly relevant to a DEMO-like reactor size, it gains a lot of interest in view of potential applicability in a future volumetric neutron source (VNS) [64] where large neutron fluence would be required to inveestigate Tritium Breeding test modules. In the case of DTE2 experiment, the scenario took advantage of the large D_{fast}-T cross-section around the 125 keV of full energy spectrum of JET NBI beam system but proved to be prone to high-Z (W) core accumulation with performances degrading gradually after 2 s approximately. Therefore it was decided to dedicate further experimental effort to mitigate the accumulation and further extend the duration of high neutron flux production. Analysis of the DTE2 scenario showed that the main causes of the W accumulation are the strong rotation and the density peaking usually observed in strongly NBI heated plamas. To mitigate these effects, given the relatively small amount of time

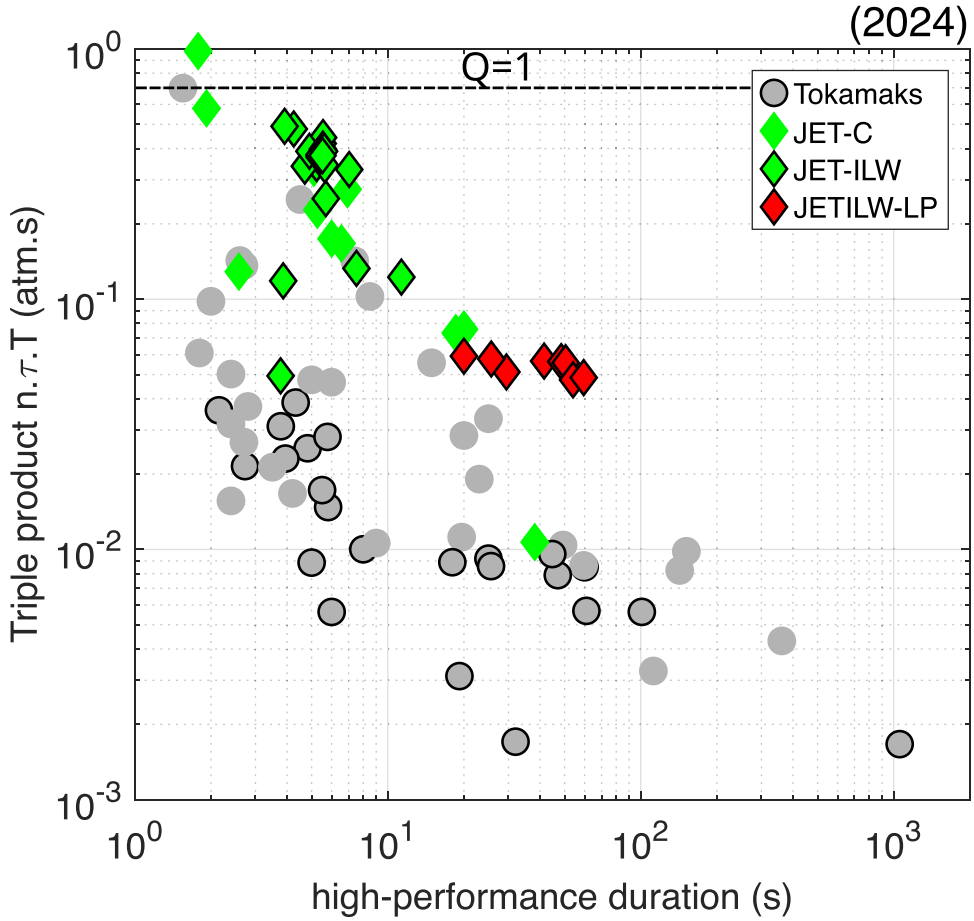

Figure 9. Triple product $n_{\mathrm{i}} \cdot \tau_{\mathrm{E}} \cdot T_{\mathrm{i}}$ versus high-performance duration for multiple devices from the CICLOP database. The dashed black line corresponds to a $Q = 1$. JET-ILW points (red diamonds) stand out, maintaining $n_{\mathrm{i}} \cdot \tau_{\mathrm{E}} \cdot T_{\mathrm{i}} \approx 0.05 - 0.06$ atm s with minimal degradation up to 60 s about five times higher than comparable-duration entries in the 2024 CICLOP dataset [61]. Reproduced from [61]. The Author(s). CC BY 4.0.

available to optimize the scenario, effort concentrated on maximizing the ICRH coupled power, because of the known ICRH beneficial effects in reducing W accumulation via increased turbulent transport as well as in reducing the density peaking [65, 66]. In addition, simulations revealed that fundamental ion cyclotron resonance heating were able to significantly increase the fusion reactivity by accelerating both the bulk and fast Deuterons' population to energies maximizing the D–T reactions rates [67]. Motivated by these simulations the T-rich plasma scenario was therefore improved, with higher ICRH coupled power (up to 5.5 MW) and reaching the new fusion energy record of 69 MJ with increase duration of the stationary phase and a fusion power of P_{fus} of 12.5 MW averaged over a 5 s period. The time traces of the attained fusion power record are shown in figure 10 together with old data from DTE1 and DTE2. For completeness in this figure we also indicated the fusion power produced in the main scenarios investigated during DTE3 and described in sections 2.1–2.4. Note that all these scenarios were never optimized nor conceived (given the machine size and heating capabilities) to maximize fusion performance, but more to explore the parameter space with the JET capabilities thus making a significant step towards D–T candidate scenario for next step. It is worth noting that, as it was the case for DTE2 [63], also the produced fusion power for the T-rich DTE3 scenario follows closely the NBI power waveform (confirming the strong beam-target contribution to the neutrons) which account for the observed oscillations [63].

A summary of the engineering parameters explored in the mentioned scenarios is provided in table 1.

3. Addressing open physics issues in view of ITER and next step devices

3.1. Screening of high-Z materials in JET-ILW plasmas

Operation with tungsten (W) PFCs entails a stringent requirement to control high-Z impurity transport, due to the potential threat of impurity core accumulation which can lead to radiative collapse and potential disruption. Therefore, demonstrating and quantifying edge temperature-gradient screening—an outward neoclassical (NC) convection driven when $(R/L_{T_{\mathrm{i}}})$ sufficiently exceeds $R/L_{n_{\mathrm{e}}}$ (see [68] for a nice overview of the effect of W in tokamak operation)—is central for viable

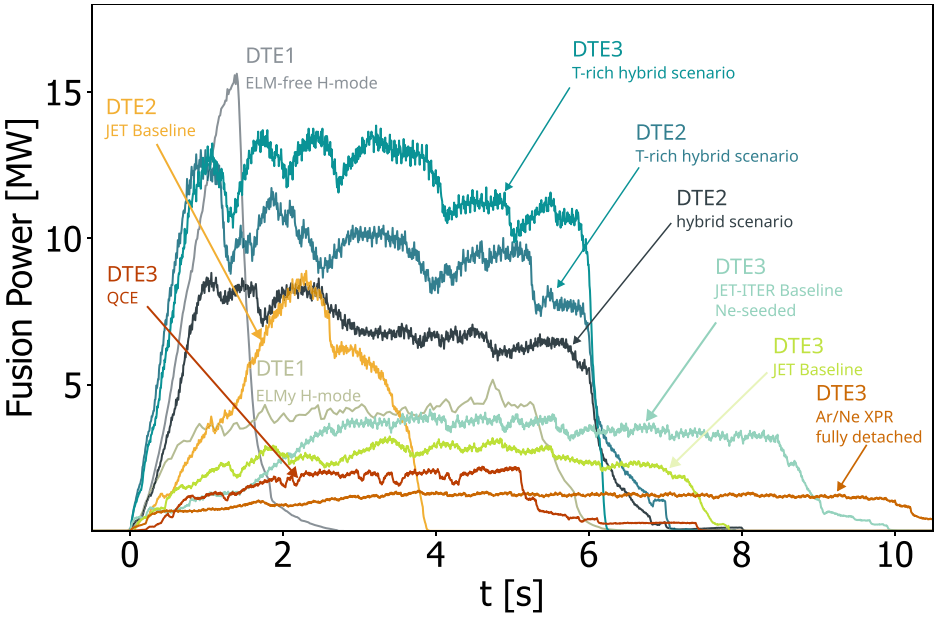

Figure 10. Time traces of fusion power for the DTE1 (ELM-free H-mode #42976 and ELMy H-mode #42982), DTE2 (hybrid scenario with $n_D \sim n_T$ # 99869, T-rich hybrid scenario # 99971 and JET baseline scenario # 99948) and DTE3 discharges (T-rich hybrid scenario # 104522, Ne-seeded ITER baseline scenario at 3.0 MA # 104 600, JET baseline scenario # 104663, QCE scenario # 104494, XPR scenario with Ar/Ne seeding and fully detached # 104296).

Table 1. Plasma parameters across different operational scenarios described in sections 2.1–2.5 and explored in JET during the last campaigns in 2022-2023. All the reported scenarios were explored both in D–D and in D–T. Some explored a wider parameter range, as indicated in the table, whereas others, due to time constraints concentrated on narrower or single operational point. The definition of the different divertor configurations refer to the position of the inner and outer strike points, with VV indicating both the strike points hitting the inner and outer vertical targets, CC with both the strike points in the corner configuration and V5C with the inner strike point on the inner vertical target whereas the outer strike point on the horizontal one. For only the JET-ITER baseline scenario, the radiation fraction reported in the table and indicated by * has been corrected to achieve power balance following the methodology available in [20], thus the value reported in the table is different from the one estimated with bolometry. A similar exercise has not yet been performed for the other scenarios which therefore does not account for potential systematic difference in radiation estimate from bolometry and/or NBI power deposition efficiency.

	JET-ITER Baseline	QCE	XPR	JET Baseline	JET/JT-60SA
B_t [T]	2.6/3.45	2.3/3.3	2.65	2.4–3.6 (3.3 in D–T)	1.7/2.4
I_p [MA]	2.5/3.2	1.5/2.25	2.5	2.5–4 (3.5 in D–T)	1.4
q_{95}	2.3/3.5	3.5/6.4	3.3	2.8–3.3	4.0/6.0
$\langle\delta\rangle$	0.35	0.45	0.22	0.1–0.2	0.42
Divertor Configuration	VV	V5C	VV		CC
P_{heat}	24–37	11/31	26/31	10–36 (27–32 in D–T)	15/25
f_{GW}	0.37/0.92	0.7/0.96	0.7–0.88	0.5–0.7	0.4/0.6
β_N	1/2.5	1/2.4	1.3/1.5	1.2–2.4	2/4
f_{rad}	0.33/0.9*		0.75	0.2–0.45	0.2/0.3

operations in any metallic devices. This screening is predicted to occur in the pedestal region of ITER plasmas [69] and has been reported in JET hybrid scenario plasmas characterized by high input power, low collisionality, and strong rotation both in deuterium [70] and in mixed isotope D–T operation during DTE2 campaign [71].

During the D–D deuterium campaign in 2022–2023 and subsequent DTE3 campaign, further optimization scenario was pursued to improve W screening studies. In D–D, optimized gas fuelling waveforms with an initial *no-gas* phase during the high-power ramp were used to build a strong temperature pedestal, followed by a timed gas puff to trigger the first ELMs and avoid an excessively large initial ELM that would bring W into the plasma and degrade pedestal performance [72]. In order to achieve an even lower pedestal density than previously attained, the initial scenario at 2.3 MA/3.45 T was further refined with a reduction of plasma current to 2.1 MA while keeping the same toroidal field allowing a larger reduction of pedestal density $n_{e,ped}$ and increase of ion pedestal temperature $T_{i,ped}$ (while keeping total heating power ≈35 MW, with $P_{NBI} \sim 30$ MW and $P_{RF} \sim 5$ MW). The explored experimental scenario was able to reduce even further the top pedestal collisionality and increase further the toroidal rotation therefore improving the favourable condition

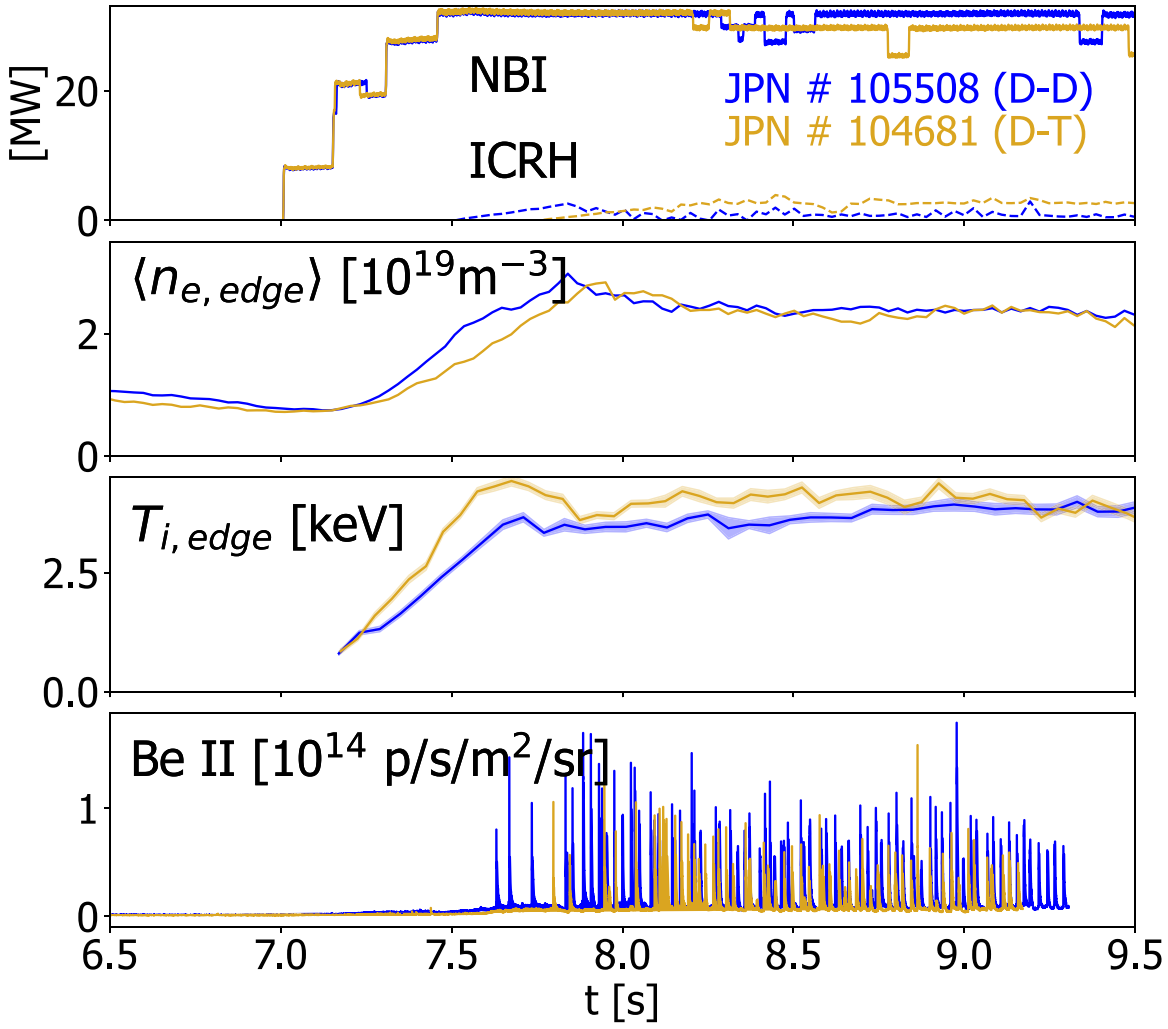

Figure 11. Time traces from a DD (blue) and a DT (gold) hybrid plasma studied for W screening. From top to bottom: NBI and ICRH power, line average density, ion temperature close to pedestal top, Be II line intensity used as ELM monitor. Both the pulses were operated at 2.85 T/2.1MA.

for high-Z impurity screening [72, 73]. A similar scenario was also explored in D–T operation, to explore the isotope dependence of NC screening as well as to improve diagnostic coverage from bolometery, avoiding the usage of main chamber gas injection which hampered bolometric measurement in DTE2. To expand the scenario in D–T plasmas while preserving the delicate H-mode entry timing (affected by the isotope dependence of the L–H threshold [74]), the toroidal field was increased to 3.85 T at the same current levels of 2.1 MA. A T-rich gas ramp compensated all-D NBI fuelling, and dry runs were used to synchronize arrival times from the different gas injectors. Time traces from the two pulses in D–D and D–T are shown in figure 11. The optimized D–T pulse JPN 104 681 (2.1 MA/3.85 T) achieved transiently an ion temperature in the excess of 4 keV inside the pedestal top ($\rho_t \approx 0.85$, during current overshoot phase of the scenario), with sustained $T_{i,ped} \approx 3$ keV during the steady ELMy phase, $\Omega_{\phi,i,ped} \approx 30$ krad s^{-1}, $f_{ELM} \sim$ 40–60 Hz, and radiated power fraction ∼20%–30%; a matched D–D pulse (JPN 105 508) at identical plasma engineering parameters provided direct isotope comparison. Notably, in the D–D to D–T scenario transfer, precise fuelling timing and avoidance of diagnostic contamination were mandatory to preserve inter-ELM analysis windows by keeping $f_{ELM} \leqslant 50$ Hz.

Screening and flushing were quantified from fast bolometry using tomographic reconstructions and line-of-sight selection that emphasizes the mantle region while excluding core contributions. As explained in [15, 70], the inter-ELM W screening metric is made of the relative change in mantle W content per ELM cycle, $(\Delta\bar{n}_W/\bar{n}_W|_{iELM})$, inferred from the flushing signal $f_{fl} = P_{rad}^{man}/\bar{n}_e$, under the approximation that the total emissivity is W-dominated and the cooling factor $\mathcal{R}_\varepsilon$ remains approximately constant over the mantle. Considering the D current scan (2.3 MA vs 2.1 MA, both at 3.45 T), the primary effect of plasma current reduction is to decrease $n_{e,ped}$ by approximately ~ 30 % leading to a similarly increase of $T_{i,ped}$. Analysis of bolometer data confirms an increase of the negative $\Delta\bar{n}_W/\bar{n}_W|_{iELM}$ by a factor of $\sim \times 2$ [15].

For matched 2.1 MA/3.85 T pulses, the D–T case showed modest inter-ELM screening with ($\Delta\bar{n}_W/\bar{n}_W|_{iELM} \approx -0.3 \pm 0.3$ %), whereas the D case demonstrated stronger screening of -2.9 ± 0.4 % [15]. Consistent with screening, flux-surface-averaged total emissivity profiles $\langle\varepsilon_{tot}\rangle(\rho)$ remained hollow across the pedestal gradient region, while the mantle volume contribution dominated total radiation due to its larger volume, even when core accumulation was modest and controlled by minority ICRH [15].

Interpretive NC modelling used the FACIT code [73], coupled to fitted kinetic profiles ($n_e, T_e, T_i, \Omega_{\phi,i}, q$) and ADAS atomic data to compute NC diffusion $D_{NC,Z}$ and convection $V_{NC,Z}$, including rotation effects. The temperature-screening coefficient C_{TS}, which enter into the definition of the NC convection $V_{NC,Z} \propto \zeta_{NC} = C_{TS}R/L_{T_i} - R/L_{n_i}$ as defined in [73], remained $\sim$ 0.3–0.5 in the core at low collisionality, but decreased (~ 0.2) in the pedestal gradient region at higher collisionality, where rotation enhances inward frictional pinch; thus the model predicted strongly inward convection across the pedestal ($V_{NC,Z} \sim -25 - 40\,m\,s^{-1}$) and near-zero convection at mid-radius, with only transient outward convection inside the core early in some pulses. Consequently, calculated W total emissivity profiles matched flux-surface-averaged tomographic reconstructions reasonably in the core balance but *did not* reproduce measured hollowness near the pedestal nor the observed inter-ELM screening across the pedestal gradient region; predicted core peaking was often stronger than observed, particularly in D at 2.1 MA/3.85 T. Sensitivity analyses indicated that modest increases in R/L_{T_i} or decreases in R/L_{n_i} can flip the sign of $V_{NC,Z}$ near mid-radius, highlighting susceptibility to profile uncertainties. Beyond FACIT's trace-impurity assumption, drift-kinetic NEO calculations were performed with experimentally relevant Ni concentrations ($\Delta Z_{eff} \sim 1$). These calculations showed that inter-species friction can drive *outward* W convection ($V_{NC,Z} \sim 1 - 15\,m\,s^{-1}$) across the outer core. This result contrasts with FACIT predictions, which neglect poloidal weighting of mid-Z collisions, which instead might play a significant role. The discrepancy suggests that mid-Z impurities may be essential to reconcile modelling with the observed inter-ELM screening. More investigation is in progress to assess if, the NC model implemented in the FACIT code version used, based on [75], is fully appropriate for the description of pedestal parameters explored in these plasma or if additional model refinement is needed [15].

3.2. Exploring low $\nu^*_{e,ped}$ regimes in JET-ILW plasmas

Predictive simulations indicate that ITER will operate with a very high pedestal electron temperature ($T_{e,ped} \approx 4 - 5$ keV) and low collisionality ($\nu^*_{e,ped} \lesssim 0.1$), with the pedestal possibly being limited by low-n peeling modes [76]. However, these predictions remain uncertain due to their sensitivity to the edge current density near the separatrix: therefore, increasing knowledge and predictive capabilities is essential given the differences expected according to the underlying limiting instabilities. Indeed in peeling-limited pedestals, the pedestal pressure is supposed to increase with both pedestal and separatrix density, in contrast to ballooning-limited pedestals, where increasing density typically degrades performance as seen in DIII-D [77]. Therefore the validation of available predictive tools in JET-ILW including isotope dependence is of paramount importance for ITER extrapolations. To date, peeling-limited pedestals have been routinely observed only in carbon-wall devices, with little evidence in metallic environments. Historically, JET-ILW pedestals have been limited by ballooning or coupled peeling-ballooning modes, even at the lowest explored collisionalities, with no clear cases of purely peeling-limited pedestals. To address this gap and assess the roles of density and isotope mass, critical for ITER predictions, a new operational strategy was implemented on JET. Guided by Europed simulations [78], this approach explored high-q_{95} operation (up to $q_{95} \approx 8.5$) by combining low plasma current (1.4 MA) with high toroidal magnetic field (from 3.4 to 3.8 T). The plasma shape was optimized in view of pumping capabilities and a low gas rate (0–1 $\times 10^{22}$ e s^{-1}) aiming to reach low density plasma. The heating power combined neutral beam injection, with power between 22–25 MW and ICRF heating with $P_{RF} \leqslant 3$ MW. A high triangularity scenario, with $\delta_{av} \approx 0.37$, was selected. The high toroidal field B_t at relatively low value of plasma current I_p stabilizes ballooning modes and enabled unprecedented JET-ILW conditions: normalized pedestal collisionality $\nu^*_{e,ped} \approx 0.15$ and normalized radius $\rho^*_{ped} \approx 0.002$, much closer to ITER's projected operational space (see figure 12) [79]. The figure illustrates the explored pedestal collisionality range as a function of normalized toroidal radius and separatrix-to-pedestal density ratio, compared with earlier high-δ cases, with indication of the different isotope composition explored. Stability analysis confirmed that the new regime was indeed peeling-limited, with low-n peeling modes limiting the corresponding pedestal pressure [14]. A density scan in peeling-limited conditions confirmed the predicted positive correlation between pedestal pressure and pedestal density. In contrast, increasing separatrix density had little effect on pedestal pressure, marking a clear difference from ballooning-limited regimes previously observed in JET-ILW [80]. JET's unique capability also enabled an isotope mass scan from pure deuterium to tritium-rich plasmas. Consistent with earlier observations, the pedestal pressure increased with isotope mass, primarily due to higher pedestal density rather than changes in pedestal temperature. However, while in the high ν^*/ballooning limited pedestal the improved pressure was due to a direct effect of the isotope mass on resisitve MHD [81], in the low ν^*/peeling limited pedestal the improved is due to the indirect effect stabilization effect provided by the increased density on peeling modes [14]. The combined information provide confidence on the achievable performances on ITER with no degradation at high $n_{e,sep}$ and a positive effect of mixed isotope operation in terms of achievable pedestal pressure. Noticeably Europed predictions captured the observed trends in pedestal pressure *versus* to both density and isotope mass, reinforcing confidence in its applicability for ITER pedestal predictions [79].

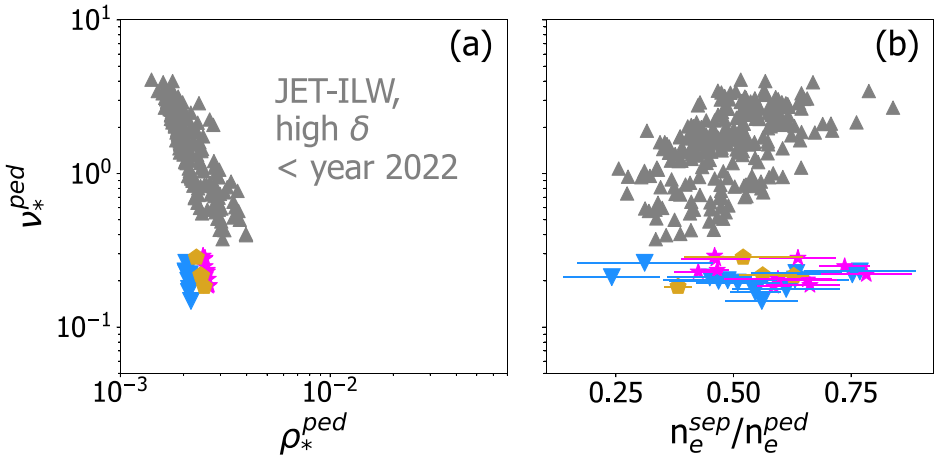

Figure 12. Ranges of pedestal collisionality as a function of normalized ion Larmor radius at the pedestal $\rho_i^{*,ped}$ (*a*) and as a function of separatrix density normalized to pedestal density (*b*). In color the explored parameter space with respect to earlier high-delta cases, depicted in gray. Colors in the new dataset indicate different isotope compositions: Deuterium (blue points), D–T (gold) and T-rich (magenta).

3.3. Fast ion dynamics and studies

JET and its unique D–T capabilities, coupled with high ICRH heating, offered the ideal test bed for advancing the understanding of the physics as well as diagnostic and control capabilities of fast ions, including alpha particles, in conditions not explored so far in any other devices. Indeed, prior to the D–T phases JET was equipped with a comprehensive set improved energetic-particle diagnostic [82] which provided the possibility for comprehensive studying of the α-particle losses.

Further progress was made in the analysis of the DTE2 experiments in support of the development and application of fast-ion diagnostics, including γ-ray spectrometers, fast-ion loss detectors (FILD), and 2D neutron/gamma cameras. A novel measurement at JET [83] established the gamma-ray-to-neutron branching ratio for the deuterium–tritium reaction. A linear correlation between γ and neutron yields was observed for deuteron energies 80 ± 20 keV, providing the validation of γ-ray spectrometry as an additional technique to monitor fusion power in ITER and future fusion power plants. The detailed analysis of the DTE2 discharges, including interpretative transport modelling, revealed evidence for electron heating by alpha-particles in the transient *afterglow* phase of high-power discharges with internal transport barrier in with NBI-only heated discharges [82]. Additionally, a new method to detect electron heating by α-particles was developed by using the dynamic response of Te to the modulation of ICRH power [84]. Investigation of α particle losses were performed, including both classical as well instability driven losses, with evidences of MHD driven losses due by fishbones, sawtooth crashes and ELMs [82]. These two loss mechanisms result in drastic, discrete, bursts of alpha particle losses with varying degrees of reproducibility and strength. On the other hand, no correlation with TAE modes were observed experimentally in any of the FILD spectrograms. This is likely due to the low alpha particle pressure produced in the JET plasmas.

Analysis of past fast-ion experiments in D–^{3}He, D–T, and H–D plasmas demonstrated the beneficial impact of MeV-range fast ions on stabilizing core turbulence and improving plasma confinement. In D–^{3}He plasmas, fast deuterons with energies $E_D \approx 1$–2 MeV were generated using ICRF and the three-ion D-(D NBI)-^{3}He scenario, leading to improved confinement in the presence of fast-ion-driven instabilities [85, 86]. Follow-up studies in D–T $\approx$ 50%–50% explored scenarios with dominant core electron heating generated by ICRF. In these experiments, hydrogen minority heating at low concentration $n(H)/n_e \approx 1\%$–1.5% was used and a range of fast-ion-driven instabilities, including TAEs, was observed. A significant reduction in the thermal ion heat conductivity in the plasma core was revealed through both power balance analysis and gyrokinetic modelling. Local and global GENE modelling identified multiple mechanisms contributing to turbulence reduction at different radial locations [87, 88]. The analysis of experimental data indicated stronger turbulence reduction by fast ions in D–T plasmas, as compared to equivalent D–D plasmas, which may be explained by nonlinear FAR3d simulations showing enhanced shear flows in the D–T cases [89]. Turbulence reduction in the presence of MeV-range fast ions and fast-ion-driven instabilities was also observed in H-D plasmas using the three-ion D–^{3}He-H ICRF scheme, where TRANSP-TORIC modelling showed over 90% of ICRF power transferred from resonant ^{3}He ions to electrons [90]. JET results complement observations on other tokamaks, including AUG, DIII-D, EAST, HL-2A, and KSTAR, and provide valuable data points for multi-machine studies and analyses, supporting the investigation of these mechanisms in future fusion devices such as ITER [91, 92].

New dedicated experiments with three-ion D-^{3}He–H scheme scenario at JET investigated the impact of ICRF antenna phasing on fast-ion behaviour and plasma dynamics [93]. The variation of antenna phasing significantly affected sawtooth periods and the spectrum of fast-ion-driven instabilities, including TAEs and reversed-shear AEs, demonstrating its potential as an actuator for plasma stability control. These results provide a valuable testbed for validating energetic particle modelling tools for ITER.

New DTE3 experiments highlighted the flexibility of ICRF for bulk ion and electron heating in D–T $\approx 50\%$–50% plasmas. At $B_0 = 3.7$ T, comparison between H-minority heating and the three-ion T-(^{9}Be)-D scheme showed that H-minority heating produced the highest electron temperatures variation ($\Delta T_{e0} \approx 1.2\,\mathrm{keV MW^{-1}}$), while the case with dominant absorption of RF power by ^{9}Be impurities resulted in the highest increase of ion temperatures ($\Delta T_i \approx 0.9\,\mathrm{keV MW^{-1}}$) [93]. Novel approaches using argon impurities were successfully tested, offering alternatives for ion heating in the absence of beryllium in the new ITER baseline [93].

During the last Deuterium campaign further progress was made in α-particle studies in plasmas without the use of tritium. In D-^{3}He plasmas, using either third-harmonic acceleration of D-NBI ions ($\omega = 3\omega_{ci}(D)$) ($B_t = 2.3$ T, $f = 51$ MHz), with n(^{3}He)/$n_e \approx$ 10%–15%, or the three-ion D-(D NBI)-^{3}He ($B_t = 3.65$ T, $f = 33$ MHz), with n(^{3}He)/$n_e \approx 25\% - 30\%$)scheme, α-particles with birth energies of ~ 3.6 MeV were generated, see figure 13. These investigations will provide information for future JT-60SA scenarios where a significant population of α-particles is expected to be generated from D–^{3}He reactions at N-NBI injection energy of 500 keV [94]. It also supports the development of new alpha-particle techniques for ITER [82]. In addition, fast-ion tomography methods were advanced for the analysis of past experiments in D-3He plasmas at JET [95].

4. Safe and reliable operation for next step devices

4.1. Disruption mitigation strategies and electron runaways

Developing strategies for effective disruption mitigation in ITER scenarios via full exploitation of the installed SPI has been one of the main scientific goals of the Deuterium 2023 campaigns on JET. This effort is critical to mitigate the severe thermal loads on PFCs and the significant EM loads induced during vertical displacement events (VDEs) [96]. Furthermore, a robust mitigation strategy is essential to prevent or safely terminate RE beams, which otherwise pose a risk of localized melting and vessel damage.

Since the JET SPI is not tritium compatible, no experiments could be planned once tritium was injected in the device thus limiting the exploitation to the experimental campaigns before DTE3. The experimental strategy and plasma discharges have been organized in key physics and technical questions essential for qualifying the SPI strategies for ITER as the material assimilation physics and thermal quench (TQ) dynamics, where the mitigation of thermal loads using SPI has been extensively characterized and validated [97]. Other topics include multiple pellet injection SPI scenarios, the influence of q-profile, intrinsic impurities and plasma instabilities on the mitigation process, the evolution of radiation asymmetries, and the effect of fragment size and velocity distributions [98].

For executing these experiments, the three-barrel SPI at JET installed in 2021 [99] was significantly upgraded to inject two identical size pellets (10 mm) and one smaller size pellet (4 mm) while controlling the velocities within the range of 200–650 m s^{-1}. The JET High Resolution Thomson Scattering diagnostic has been upgraded for measuring temperatures in the low eV range [100] when the injected pellet fragments are cooling the plasma thus allowing the measurements of the effects on plasma density, temperature and radiation. In addition, the fragment penetration has been monitored by fast cameras.

The last JET SPI campaign delivered novel experimental results focusing on the impact of seeded impurities (as N_2 or Ne exploited in the seeded scenarios described in section 2.1) on the mitigation efficiency with SPI [101]. This research addresses a critical scenario for future reactors like ITER, which will employ impurity seeding for enhanced power handling. The primary finding is that for pure D SPI, increased impurity seeding led to an order of magnitude reduction in the pre-thermal quench (pre-TQ) duration (from $\sim$70 ms down to $<$ 10 ms). This drastically reduces the crucial time window required for the initial D injection in the envisaged, so called, staggered SPI schemes (when two pellets are launched from single injector) designed to suppress RE generation. Importantly the experiments demonstrated the robustness of single mixed neon/D SPI, as no reduction in the overall thermal load mitigation efficacy (inferred via radiated energy fraction as seen in figure 14) was observed across the range of seeding levels tested.

The first interpretative and quantitative 3D non-linear MHD modelling of pure D SPI into a JET H-mode plasma using the JOREK code has been carried out [102, 103]. The plasma target for these simulations was a 3 MA / 7 MJ discharge. This work identified and quantified two crucial physics effects for accurate prediction of disruption mitigation efficacy: the drift of ablation plasmoids and the role of background impurities (ie W). The simulations showed that the outward drift of ablated material towards the LFS (a movement related to the trajectories illustrated in figure 15) results in approximately 70% reduction in core density rise. This significant reduction suggests that relying solely on D SPI from the LFS may be limited in achieving the high core density necessary for effective RE avoidance in large-scale devices. Furthermore, the study confirmed that even low levels of pre-existing impurities in the background plasma were sufficient to dominate the radiative cooling and MHD activity that triggers the TQ.

To investigate the potential threat of a non-uniform radiation pattern as a consequence of radiating impurities injected by SPI, dedicated experiments were performed on JET to quantify this potential radiation asymmetry [104]. Such asymmetries could result in intense localized photon flashes during the thermal quench. The toroidal peaking factor (TPF), defined in [104], was used as a figure of merit for representing the toroidal uniformity of the radiation. The TPF proved to decrease with increasing plasma stored energy, with a maximum at the injection SPI point. The observed decrease with increased plasma energy suggests a favourable scaling towards ITER. Furthermore, in ITER multiple toroidal injections are planned, thus further improving the toroidal spread of the radiation during the thermal quench.

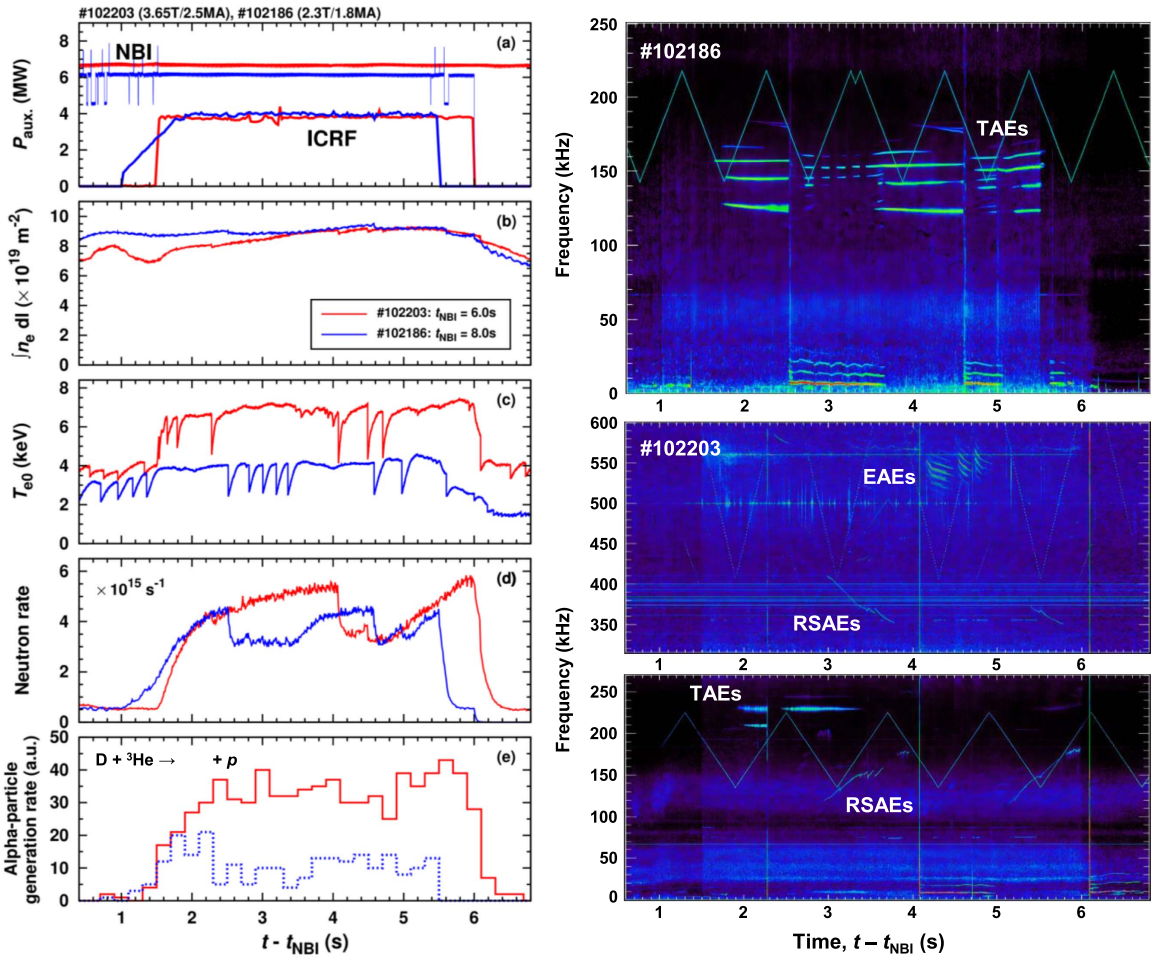

Figure 13. Overview of fast-ion experiments in D-3He plasmas, in which a significant population of α-particles was generated using a combination of D-NBI and ICRF. Red traces correspond to pulse JPN 102 203 (3.65 T/2.5MA), employing the three-ion D-(D_{NBI})-^{3}He scheme with $n(^3\mathrm{He})/n_e \approx 25\%$–$30\%$. Blue traces correspond to pulse JPN 102 186 (2.3 T/1.8MA), using the 3rd harmonic deuterium, $\omega = 3\omega_{ci}(\mathrm{D})$ scheme with $n(^3\mathrm{He})/n_e \approx$ 10-15%. The right-hand panel illustrates the rich variety of fast-ion-driven instabilities observed in these experiments.

The low-Z benign termination scenario [105] has been recognized as a promising safe route for minimizing the consequences of RE. It works by injecting large amounts of D_2 or H_2 into the RE beam and leads to an almost complete suppression of heat loads at impact. The low-Z injection can be made by SPI, massive gas injection (MGI) or standard gas fuelling valves, although the latter is likely not to be a viable solution for devices the size of ITER and beyond. Low-Z injections make the companion plasma recombine down to free electron density values below $10 \times 10^{18}\,\mathrm{m}^{-3}$. This recombined state has been shown to be strongly linked to the success of this scheme [106].

During the JET D–D phase in 2023, the boundary of the operational space for the low-Z RE benign termination scenario has been investigated. It was shown that sufficient amount of deuterium is needed to achieve recombination and reach benign termination. These results sit within a multi-machine global database, including data from AUG, COMPASS, DIII-D, and TCV, which identifies a critical neutral pressure window required for successful recombination and establishes the scaling of these limits with RE current density and high-Z impurity levels [107]. This effect will need to be further studied with modelling as it is critical for the safe mitigation of RE beams in ITER.

On the last day of JET experiments, a high current ($\sim$1.7MA) unmitigated RE beam was produced, by injection argon into a 3MA plasma and terminated intentionally onto the JET beryllium inner wall (see figure 16). This experiment, was designed to produce data for ITER such as impact angles, wetted area, pitch angle, RE energy... for modelling beam propagation into plasma facing components [108] and extend the previous work as described in [109].

4.2. Real-time control implementation compatible with D–T operation

During the last D–D and D–T operation in 2022 and 2023, several advanced RT controllers were implemented and deployed with the specific target of being compliant with D–T operation. These developments targeted isotope ratio control, H-mode

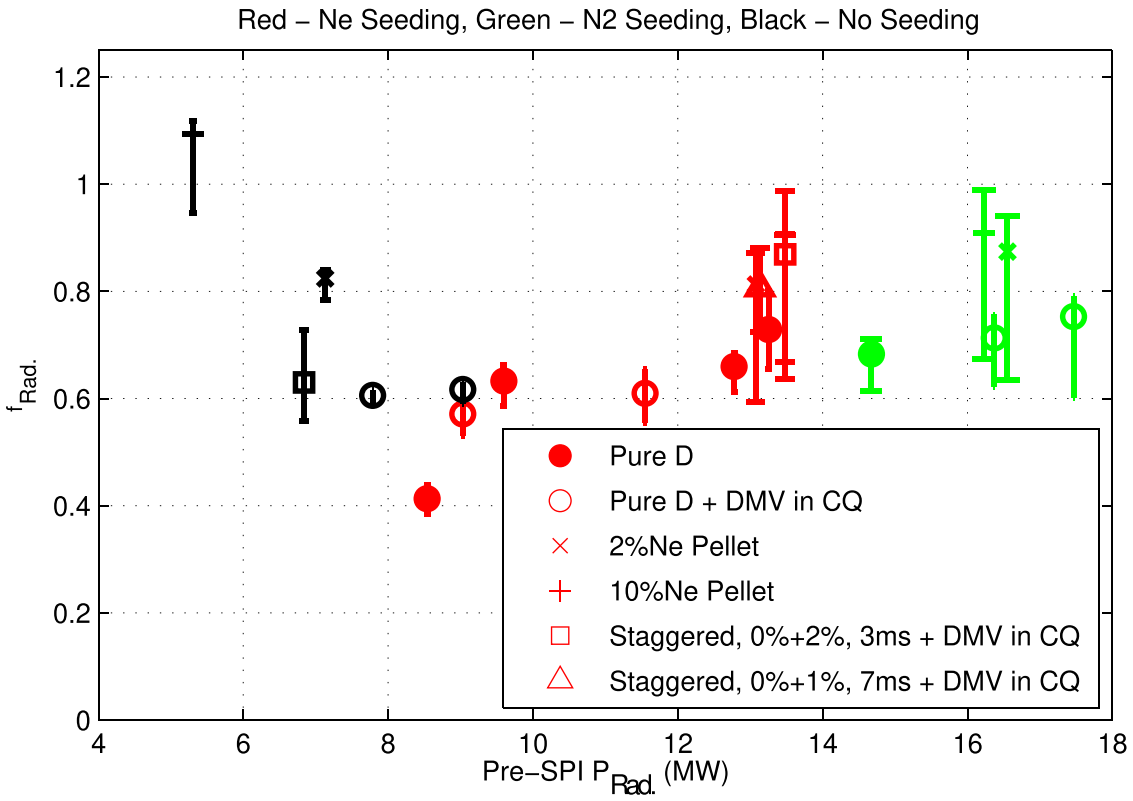

Figure 14. Radiated energy fraction as a function of pre-SPI PRad. for a range of SPI compositions. Reproduced from [101]. The Author(s). CC BY 4.0.

management including entry and exit, divertor detachment, and detection of underperforming discharges, with direct applicability to next step devices.

Closed-loop control of the D:T ratio was demonstrated under H-mode conditions using gas valves for tritium and gas or pellet injection for deuterium [110]. The RT controller, using spectroscopic measurements of T/(T+D) ratio in the divertor as observer, proved to be efficient to adjust plasma composition from D-rich to T-rich [110]. The tritium was injected via gas valves, while deuterium injected either via gas valves or pellets. In this JET (I_p = 1.41.4 MA, B_T = 1.7 T) scenario, NBI core fuelling accounts for less than 10% of the total fuelling. Fusion power, measured via neutron rate, responded promptly, confirming efficient core-edge mixing as described in [111]. This demonstrates that, although the plasma is fueled mainly at the edge, rapid mixing of the isotopes occurs throughout the plasma up to the core and that controlling the D:T ratio is an effective way of controlling the burn rate. In addition, a multi-input multi-output controller combined isotope ratio regulation with ELM frequency control, maintaining stability during fuelling variations as shown in figure 17. This constitutes the first demonstration of simultaneous decoupled control of burn rate and edge stability in a D–T plasma.

As described in section 2.3 an extensive work devoted to the implementation of the RT control of the XPR position was done. A PI controller was designed from dedicated system-identification experiments, using the horizontal bolometry line of sight through the *X*-point as sensor, and Ar gas injectors as actuator, thus maintaining compatibility with D–T operation [36]. In these preliminary experiments, a very clear response of the XPR height was observed with the injection of argon but not with neon, thus providing a viable path towards a stable solution. Notably the implementation of the controller on JET, strongly benefitted from previous analogous studies in medium size tokamaks [39]. Experiments at I_p = 2.5 MA, B_T = 2.7 T, and P_{input} = 20–30 MW achieved stable XPR positioning holding the maximum radiation at the desired height position despite significant actuator delays due to the gas injection response and impurity-pumping limits. Perturbative studies confirmed isotope-independent dynamics, enabling direct transfer of controllers from D–D to D–T operation. This indicates that the design and testing of an XPR controller for a future power plant may be done during DD commissioning and directly ported to D–T operation without further tests thus reducing the required commissioning time in D–T.

With an effort already started during the DTE2 operation, all DTE3 operation at JET benefitted from a dedicated RT *dud detector*, empirically designed to control the consumption of tritium and limit the neutron budgets by keeping the target plasma performance [112]. In addition during DTE3 operation a P_{LH} based controlled was implemented regulating the ratio of the power crossing the separatrix to the L–H threshold from Martin's scaling law [113]. The detector was ensuring simultaneously that the power was sufficient to access and maintain the H-mode as well as to identify the approach to conditions prone to excessive radiation fraction close to unity. The detector proved useful to control NBI power and gas flow rate during

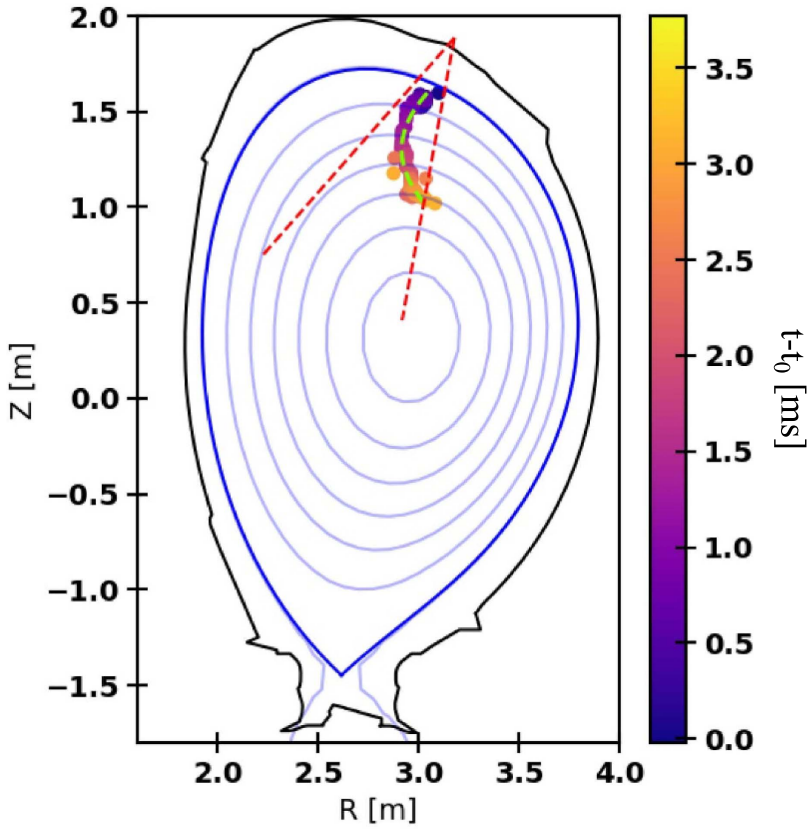

Figure 15. Tracked inboard edge of the SPI plume based on the maximum gradient of the D_α emission intensity detected by the KL8 fast camera in JET # 96874. Time in milliseconds shown in the colorbar is shifted by $t_0 = 9.039$ s, i.e. the time when the first group of fragments arrive at the plasma. Outlines of the expected SPI plume from the injection geometry are shown by the red dashed lines. Reproduced from [102]. The Author(s). CC BY 4.0.

H-mode termination and ramp-down, thus avoiding radiative collapse.

4.3. Cleaning procedure and fuel retention in JET

In next-step fusion devices, in-vessel tritium inventory must be strictly limited for safety, as well as minimized for fuel cycle efficiency. Fuel retention in PFCs can be assessed using complementary techniques:

(i) **Gas balance** between injected and pumped gas, providing global retention estimates per pulse or per day [114].
(ii) **Post-mortem analysis** of retrieved samples, yielding campaign-integrated *ex situ* local measurements and giving insight on retention mechanisms at play (see [115, 116] for instance).
(iii) **Laser-based diagnostics**, enabling local *in situ* measurements, either during campaigns or vent-phase [117].

Gas balance in JET demonstrated a 10× reduction in fuel retention when transitioning from carbon to Be-W walls [118]. In deuterium operation phase of JET-ILW, gas balance indicated short-term retention of 2% of injected fuel [118], while post-mortem analysis showed that ∼0.2% is retained long-term, mainly via codeposition of D with Be [115]. The difference between results from gas balance and post mortem analysis is attributed to long term outgassing of fuel from the wall materials [115, 118] (in-vessel outgassing as well as outgassing during sample storage). Results of post-mortem analysis demonstrate that a significant amount of long-term retained fuel is accumulated in co-deposited Be layers, especially on the upper tiles of the inner divertor ([115] and references therein). In addition to fuel retention studies in deuterium, JET enabled unique investigations of fuel retention in DT plasmas [4], including assessment of tritium removal efficiency by different techniques in the subsequent clean-up campaigns [119–122]. This is key for getting insight on fuel retention and removal for future fusion devices using a DT mix.

In campaigns involving tritium performed during the JET ILW, the amount of T injected for fuelling the plasma (364 g of T injected in total for DTE2 and DTE3, including the pure T phase before/after DTE2 [123]) was significantly larger than during the JET C phase (35 g of T for DTE1 [4]). This, however, should be put in perspective with D fuelling, which is by far dominant when integrating over the JET-ILW exploitation period. For instance, over the last period of exploitation of the JET ILW without in vessel intervention, including both DTE2 and DTE3 (2019–2023), the D injection was ∼15 times higher than T injection, as shown in table 2. Dedicated hydrogen campaign have also been done before DTE2 as well as mixed D/H and H/T experiments in view of understanding

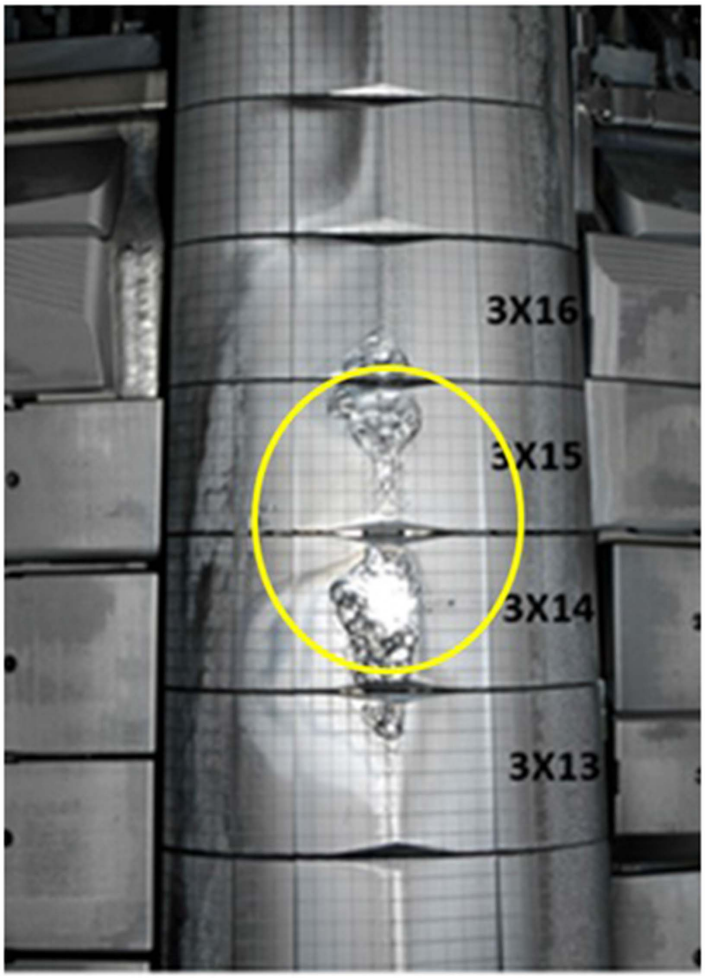

Figure 16. Intentional runaway impact on inboard Be limiter done in the last JET life pulse.

the isotopic effect on plasma transport, confinement and SOL physics. Protium was also injected regularly to ensure an optimal H/D isotopic ratio when ICRH minority heating schemes was used, and it is therefore also included in table 2. In addition, H is also present in the vessel walls from the 'natural' H loading when components are exposed to air during vessel vent. The JET vessel walls are therefore expected to be loaded with the 3 hydrogen isotopes.

All three fuel retention measurements techniques quoted above were applied during the DTE2 and DTE3 campaigns. Gas balance over full-day operations proved challenging due to low retention levels and the additional complexity linked to tritium handling within the Active Gas Handling System (AGHS) of JET (requiring use of tritium compatible gas pumping routes and associated procedures), which prevented an accurate gas balance procedure used during deuterium campaigns from being repeated. In addition, plasma operation involving He or CD4 prior to gas balance experiments, as well as the presence of residual H in the wall led to significant uncertainties in the assessment of the T retained in the vessel (see [119, 123] for details). Nevertheless, results indicate comparable fuel retention in D and DT plasmas [119, 123]. Faster decay of the post-pulse outgassing for T as compared to D suggests that the isotopes concentration depth profiles in the vessel walls may play a role [119]. Indeed, given the history of JET wall loading, T is expected to be located in the near surface of the plasma facing components, while the dominant D reservoir is expected to extend further towards the bulk material.

The global T accountancy by the AGHS is still ongoing for DTE2 and DTE3. Sample retrieval was completed in summer 2025 and post-mortem analysis is still ongoing. The efficiency of various T removal techniques was investigated thoroughly after DTE2 [120, 121], with a sequence of vessel baking at increased vessel wall temperature (320 °C as compared to normal operational temperature of 200 °C), glow discharge cleaning (GDC), ion cyclotron wall conditioning (ICWC), and plasma operation in D in various limited/diverted magnetic configurations to heat and outgas the fuel trapped in co-deposited Be layers and other components. In particular, a dedicated configuration with the inner strike point located on the tile of the inner divertor where the highest fuel content

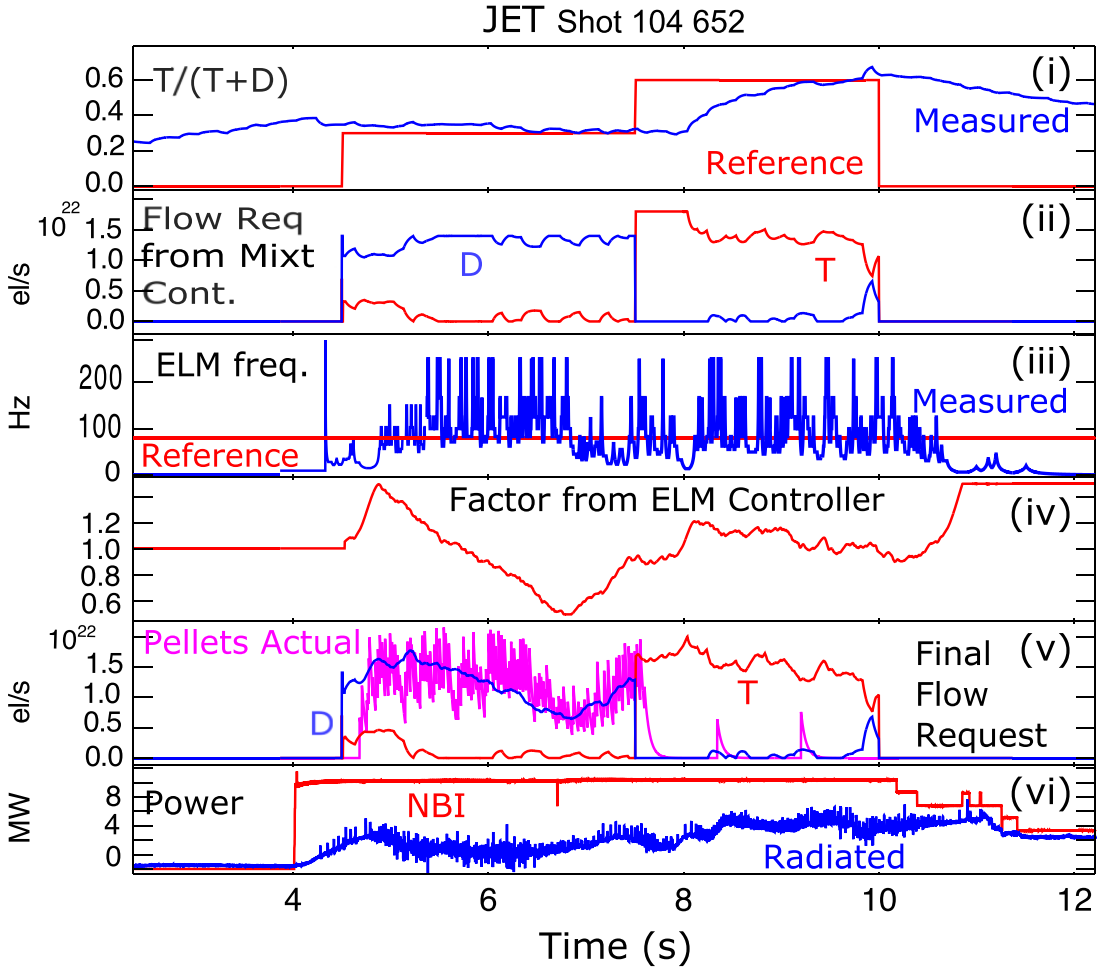

Figure 17. Combined ELM frequency and tritium fraction con-trol using pellets for deuterium and gas for tritium injection as actuator.Tritium and deuterium flow requests from the isotope controller(ii) are multiplied by the factor produced by the ELM frequency controller (iv) to generate the flow requests (*v*). Reproduced from [110]. CC BY 4.0.

was evidenced from post mortem analysis, the so called RISP (Raised Inner Strike Point), was developed in D–D. Detailed analysis of the DTE2 clean-up is published in [120]. After DTE3, the objectives of tritium clean-up were to reduce tritium concentration below 1% in the plasma (thus allowing low neutron rate deuterium operation), and the reduction of the tritium content in the exhaust gas below 0.02% (allowing the return the AGHS system into standard operation without tritium). Based on the feedback from the post-DTE2 cleaning, a sequence involving baking, ICWC and plasma operation with D was carried out, allowing to reach within 6 weeks the target T concentration in the exhaust gas (0.02%) [119, 123]. This is illustrated in figure 18, showing the time evolution of the T concentration in the plasma during the 4 weeks of D plasmas clean up, following the first 2 weeks with baking and ICWC carried out after DTE3 [119]. Redundant measurements methods were used to increase reliability on the measurements of the T concentration. Spectroscopic measurements such as optical Penning gauge spectroscopy in the plasma exhaust gas, spectroscopic Balmer lines measured in the divertor as well as neutron measurements to indirectly infer the tritium concentration [120].

Table 2. Injected hydrogen isotopes (hydrogen, deuterium, tritium) in the experimental campaigns performed in JET-ILW during the last operation period (2019–2023). Numbers given here include the gas injected into the vessel via the gas injection system, as well as via the Neutral Beam Injectors. They do not include fuelling by pellets nor by the disruption mitigation system i.e. SPI or MGI(numbers taken from [123]).

Isotope	Gas injected (atoms)
H	10^{26}
D	1.2×10^{27}
T	7.2×10^{25}

Extensive *in-situ* surface analysis using two laser-based diagnostic techniques conceived for assessing fuel retention in ITER has been performed in DTE3, including the subsequent cleaning campaign and following D operation. The Laser Induced Desorption with gas detection using Quadrupole Mass Spectrometers (LID-QMS) system was used to monitor the weekly evolution of fuel retention in co-deposited layers on specific inner divertor tiles [122, 124]. This demonstrated the capability of LID-QMS to discriminate D and T and to

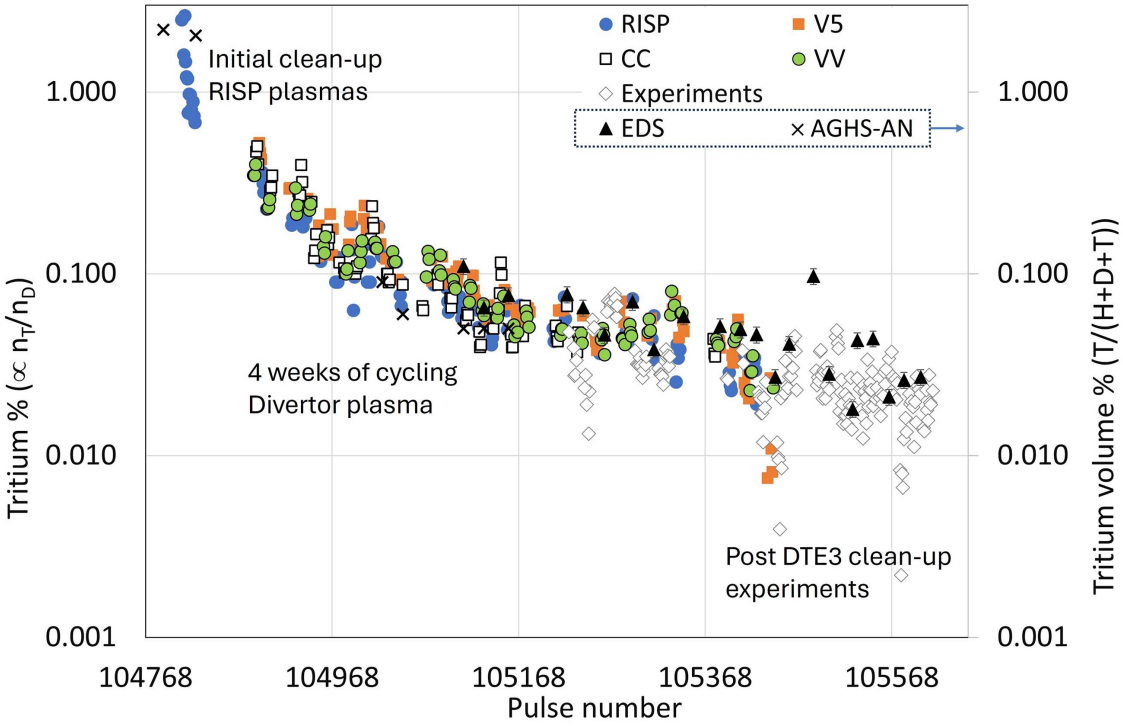

Figure 18. Evolution of Tritium concentration during the 4 weeks of DT clean-up following the DTE3 campaign, as derived from the fraction of DT neutrons to DD neutrons measured by neutron diagnostics (Reproduced from [119]. The Author(s). CC BY 4.0.). The clean-up plasmas (shown in color) include corner-corner 'CC', vertical-tile 5 'V5', raised inner strike point 'RISP' and vertical-vertical 'VV'configurations, as described in [119]. 'Experiments' plasmas, shown as grey diamonds, were interleaved with clean up plasmas at the end of the clean-up phase and are using a large variety of configurations. 'AGHS-AN' and 'EDS' correspond to measurements from two analysis systems located in AGHS to assess T concentration in the exhaust gases.

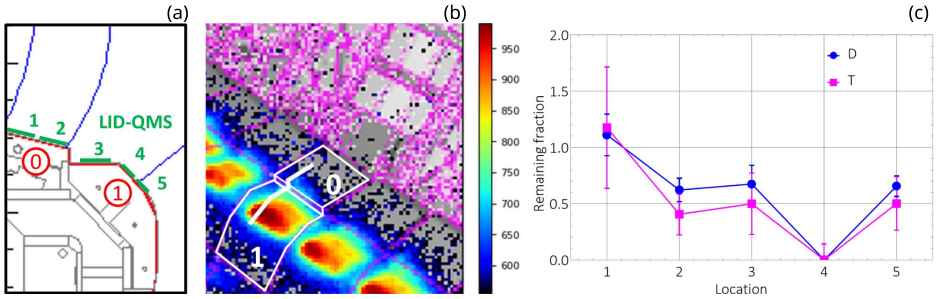

Figure 19. Change in fuel retention at the JET inner divertor following the Raised Inner Strike Point (RISP) plasma configuration. (*a*) Location of the poloidal LID-QMS scans (green numbers from 1 to 5). Inner strike point location for the RISP configuration is shown at the upper end of location 5 where the highest heat flux is expected (see [119] for details on RISP). (*b*) Infrared view during RISP operation, showing the most heated areas on tile 1(reproduced from [56]) (*c*) remaining fraction of D and T after RISP cleaning at the locations shown in (*a*), calculated as the ratio between LID-QMS measurements before and after RISP. Post RISP measurements of D/T at location 4 are below the detection limit of LID-QMS (LID-QMS data taken from [123]). (*b*) Reproduced from [119]. The Author(s). CC BY 4.0.

quantify the effect of cleaning procedures, such as operating D plasmas in the RISP configuration [119, 122–124]. Figure 19 illustrates the latter point, showing the LID-QMS measurements of the relative fraction of T and D retained at various location of tile 0 and tile 1 of the JET inner divertor performed before/after RISP operation [119, 123]. It is shown that while T/D were not released at location 1 on tile 0 (see figure 3 inset where Tile location and corresponding numbering are indicated), located away from the RISP strike point position, but roughly half of T/D was cleaned by RISP at location 2, 3 and 5 on tile 1. Finally, full fuel removal was observed at location 4, with T/D content falling below the detection limit of LID-QMS after RISP. This is roughly consistent with the highest heat flux expected between location 4 and 5 in the RISP configuration. In addition, *ex-situ* post-mortem analysis of PFC samples after removal from the JET vessel, as was done following the first JET-ILW deuterium operations in 2011–2016 [115, 125–127] will be compared to the LID-QMS measurements.

Laser induced breakdown spectroscopy (LIBS) was applied for the first time in a DT environment following the end of JET exploitation in fall 2024 [128–130]. It was deployed post-vent in the vessel using the JET remote handling arm under

atmospheric pressure with an argon flow in the measurement head. Although T detection was challenging due to low residual T levels after cleaning campaigns and due to D–T spectral lines overlap, preliminary results show that Be deposition patterns are consistent with previous observations and that there is a correlation between D content and Be layer thickness. The lessons learned during JET DT fuel retention experiments, detailed in [119], will be used to inform the strategy for T accountancy in ITER, and the design of the associated diagnostics and operational procedures (see section 4 in [131]). The extensive use of LID-QMS and LIBS, combined with the effort required for quantitative interpretation, also provides critical operational experience for ITER and are informing design of propose laser-based T diagnostic for T accountancy [132]. More details on the status of fuel retention studies in JET DTE3 can be found in [123].

5. Conclusion

The final JET campaigns, conducted within the EUROfusion Tokamak Exploitation framework, have delivered a comprehensive set of results that significantly strengthen the scientific and technological basis for ITER and DEMO. These campaigns demonstrated ITER-relevant integrated scenarios with impurity seeding, achieving partial divertor detachment and high confinement in D–T plasmas, while validating advanced exhaust solutions such as the XPR and QCE regimes in both D–D and D–T. Extensive studies of pedestal stability, including the first observation of peeling-limited pedestals in a metallic environment at collisionalities approaching those of ITER, provide critical benchmarks for predictive models. Investigations of isotope effects, impurity screening in hybrid scenarios, and turbulence suppression by fast ions have deepened understanding of core–edge integration and transport physics. Operational milestones included the achievement of a new world record of 69 MJ of fusion energy in tritium-rich hybrid plasmas, long-pulse H-mode operation sustained for 60 s, and the deployment of advanced RT control systems for isotope ratio regulation and plasma exhaust management. In addition, during the D–D campaign the experiments with the SPI have been instrumental in understanding issues like the role of the fragment size, how to optimized the assimilation of the injected materialand the robutsnesss of the SPI scheme in various scenario conditions. SPI mitigation of run-away beams have also been tested successfully up to the maximum pre-disruption current (3MA). These achievements were complemented by advances in tritium retention studies using gas balance, post-mortem analysis, and ITER-relevant laser diagnostics (LID-QMS and LIBS), providing essential input for tritium accountancy and fuel cycle strategies. Collectively, these results validate several ITER operational concepts, inform DEMO design choices, and deliver critical experience in nuclear operation, scenario optimization, and integrated control. For ITER, the successful test of steady state high performance plasma with a valid exhaust solution are calling for an increased combined effort on core-edge integrated modelling to understand these scenarios with the aim of increasing the reliability ITER predictions. This should include strengthening the modelling of pedestal in the peeling regime which the JET data have unveiled. The understanding of the physics basis for the no-ELM regimes like the QCE or the XPR regimes is also essential for producing viable DEMO scenario: noteworthy both these scenarios are also considered as a potential options for ITER $Q = 10$ operation. The experiment on disruption and run-away mitigation have produced a very large database which participate to the design and future operation of the ITER DMS. However, there remains uncertainties in extrapolating present results to ITER and modelling using 3D-MHD codes such as JOREK are therefore important on-going activities. JET's legacy, still under active data analysis and modelling activities, now provides a robust experimental foundation for the next generation of fusion devices, bridging the gap between present-day tokamaks and burning plasma reactors.

Acknowledgments

This work has been carried out within the framework of the EUROfusion Consortium, funded by the European Union via the Euratom Research and Training Programme (Grant Agreement No. 101052200 - EUROfusion). The Swiss contribution to this work has been funded by the Swiss State Secretariat for Education, Research and Innovation (SERI). Views and opinions expressed are however those of the author(s) only and do not necessarily reflect those of the European Union or the European Commission or SERI. Neither the European Union nor the European Commission nor SERI can be held responsible for them.

ORCID iDs

N. Vianello 0000-0003-4401-5346
E. Joffrin 0009-0008-7527-0984
A. Hakola 0000-0003-1385-1296
A. Kappatou 0000-0003-3341-1909
D. Keeling 0000-0002-3581-7788
B. Labit 0000-0002-0751-8182

References

[1] Rimini F.G. (JET Contributors, EUROfusion Tokamak Exploitation Team) 2025 40 years of JET operations: a unique contribution to fusion science *Plasma Phys. Control. Fusion* **67** 33001
[2] Joffrin E. *et al* 2019 Overview of the JET preparation for deuterium-tritium operation with the ITER like-wall *Nucl. Fusion* **59** 112021
[3] Jacquinot J. *et al* 1999 Overview of ITER physics deuterium-tritium experiments in JET *Nucl. Fusion* **39** 235–53
[4] Andrew P. *et al* 1999 Tritium retention and clean-up in JET *Fusion Eng. Des.* **47** 233–45
[5] Matthews G.F. *et al* 2011 JET ITER-like wall — overview and experimental programme *Phys. Scr.* **T145** 14001
[6] Maggi C.F. *et al* 2024 Overview of T and D–T results in JET with ITER-like wall *Nucl. Fusion* **64** 112012

[7] Garcia J. (JET Contributors) 2025 Importance of the second D–T campaign at JET for future fusion tokamak devices *Rev. Mod. Plasma Phys.* **9** 10

[8] Joffrin E. *et al* 2024 Overview of the EUROfusion tokamak exploitation programme in support of ITER and DEMO *Nucl. Fusion* **64** 112019

[9] Kappatou A. *et al* 2025 Overview of the third JET deuterium-tritium campaign *Plasma Phys. Control. Fusion* **67** 45039

[10] Hakola A. *et al* 2024 Helium plasma operations on ASDEX upgrade and JET in support of the non-nuclear phases of ITER *Nucl. Fusion* **64** 096022

[11] Faitsch M. *et al* 2025 The quasi-continuous exhaust regime in ASDEX Upgrade and JET *Nucl. Mater. Energy* **42** 101904

[12] Bernert M. *et al* 2025 X-point radiation: from discovery to potential application in a future reactor *Nucl. Mater. Energy* **43** 101916

[13] Garzotti L. *et al* 2019 Scenario development for D–T operation at JET *Nucl. Fusion* **59** 76037

[14] Frassinetti L. *et al* 2026 Effect of density on peeling limited pedestals in JET-ILW, MAST-U and TCV and implications for ITER pedestal predictions *Nucl. Fusion* **66** 056028

[15] Field A. *et al* 2026 Optimised 'hybrid' scenario H-mode plasmas for w radiation control in JET with the be/w wall *Nucl. Fusion* **66** 036018

[16] King D.B. 2024 JET Machine Operations in T&D-T *Nucl. Fusion* **64** 106014

[17] Pitts R.A. *et al* 2019 Physics basis for the first ITER tungsten divertor *Nucl. Mater. Energy* **20** 100696

[18] Giroud C. *et al* 2015 Progress at JET in integrating ITER-relevant core and edge plasmas within the constraints of an ITER-like wall *Plasma Phys. Control. Fusion* **57** 035004

[19] Giroud C. *et al* 2024 The core–edge integrated neon-seeded scenario in deuterium–tritium at JET *Nucl. Fusion* **64** 106062

[20] Matthews G.F., Silburn S.A., Challis C.D., Eich T., Iglesias D., King D. and Sieglin B. (JET Contributors) 2017 Dynamic power balance analysis in JET *Phys. Scr.* **T170** 014035

[21] Marin M., Citrin J., Giroud C., Bourdelle C., Camenen Y., Garzotti L., Ho A and Sertoli M (JET Contributors) 2023 Integrated modelling of neon impact on JET H-mode core plasmas *Nucl. Fusion* **63** 016019

[22] Zotta V.K. *et al* 2025 The ITER baseline scenario on JET in D-T with neon seeding *Proc. 51st EPS Conf. on Plasma Physics, Vilnius, Lithuania* vol. 51A p 1.048

[23] Hu Q. *et al* 2026 Effects of neon seeding on high-performance deuterium JET-ITER baseline H-mode plasmas: experimental results and modelling *Nucl. Fusion* **68** 055030

[24] Sos M. *et al* 2025 The impact of neon seeding on pedestal performance and stability of JET-ILW deuterium H-mode discharges *Nucl. Fusion* **68** 015018

[25] Nyström H. *et al* 2025 Effect of neon seeding on the pedestal structure and stability in the JET-ILW deuterium JET-ITER baseline scenario using both ideal and resistive MHD *Nucl. Fusion* **66** 026039

[26] Carine G. *et al* 2025 High performance ELM-free semi-detached scenario sustained at high-current in JET DTE3 *Proc. 30th IAEA Fusion Energy Conf. (Chengdu, China)*

[27] Faitsch M. *et al* 2021 Broadening of the power fall-off length in a high density, high confinement H-mode regime in ASDEX Upgrade *Nucl. Mater. Energy* **26** 100890

[28] Harrer G.F. *et al* 2022 Quasicontinuous exhaust scenario for a fusion reactor: the renaissance of small edge localized modes *Phys. Rev. Lett.* **129** 165001

[29] Dunne M., Faitsch M., Radovanovic L. and Wolfrum E. (ASDEX Upgrade Team) 2024 Quasi-Continuous exhaust operational space *Nucl. Fusion* **64** 124003

[30] Labit B. *et al* 2019 Dependence on plasma shape and plasma fueling for small edge-localized mode regimes in TCV and ASDEX Upgrade *Nucl. Fusion* **59** 086020

[31] Sun H. *et al* 2025 Impact of the plasma boundary on machine operation and the risk mitigation strategy on JET *Nucl. Fusion* **65** 076012

[32] Faitsch M. *et al* 2025 The quasi-continuous exhaust regime in JET *Nucl. Fusion* **65** 024003

[33] Dunne M.G. *et al* 2025 The physics of ELM-free regimes in EUROfusion tokamaks *Nucl. Fusion* submitted

[34] Glöggler S. *et al* 2019 Characterisation of highly radiating neon seeded plasmas in JET-ILW *Nucl. Fusion* **59** 126031

[35] Bernert M. *et al* 2017 Power exhaust by SOL and pedestal radiation at ASDEX Upgrade and JET *Nucl. Mater. Energy* **12** 111–8

[36] Bosman T.O.S.J. *et al* 2025 X-point radiator control and its dynamics in ASDEX Upgrade and JET deuterium–tritium discharges *Nucl. Fusion* **65** 016057

[37] Drenik A. *et al* 2019 Evolution of nitrogen concentration and ammonia production in n2-seeded H-mode discharges at ASDEX upgrade *Nucl. Fusion* **59** 046010

[38] Huber A. *et al* 2022 The radiated power limit in impurity seeded JET-ILW plasmas *Nucl. Mater. Energy* **33** 101299

[39] Bernert M. *et al* 2023 The x-point radiating regime at ASDEX upgrade and TCV *Nucl. Mater. Energy* **34** 101376

[40] Poletaeva A., Rozhansky V., Kaveeva E., Korzueva V., Senichenkov I., Veselova I., Pitts R. and Bonnin X. 2024 First SOLPS-ITER modelling of an x-point radiator in ITER *Nucl. Fusion* **64** 126038

[41] Nunes I. (JET Contributors) 2015 Plasma confinement at JET *Plasma Phys. Control. Fusion* **58** 14034

[42] Mailloux J. *et al* 2022 Overview of JET results for optimising ITER operation *Nucl. Fusion* **62** 042026

[43] Loarte A. *et al* 2025 The new ITER baseline, research plan and open R&D issues *Plasma Phys. Control. Fusion* **67** 65023

[44] Zotta V.K. *et al* 2022 Fusion power predictions for $\beta_N \approx 1.8$ baseline scenario with 50-50 d-t fuel mix and NBI injection in preparation to D-T operations at JET *Nucl. Fusion* **62** 076024

[45] Garzotti L. *et al* 2025 Development of high-current baseline scenario for high deuterium–tritium fusion performance at JET *Plasma Phys. Control. Fusion* **67** 75011

[46] Telesca G. *et al* 2024 COREDIV simulations of D and D–T high current–high power baseline pulses in JET-ITER like wall *Nucl. Fusion* **64** 066018

[47] Wendler N. *et al* 2024 Impurity behaviour in JET high-current baseline scenario for deuterium, tritium and deuterium-tritium plasmas *Nucl. Mater. Energy* **41** 101743

[48] Zotta V.K. *et al* 2022 Predictive modelling of D-T fuel mix control with gas puff and pellets for JET 3.5 MA baseline scenario *Proc. 48th EPS Conf. on Plasma Physics* vol 46a p 2a.115

[49] Leoni C. *et al* 2024 Scrape-off layer opacity to D and T gas puff fuelling in JET baselinescenario *Proc. 50th EPS Conf. on Plasma Physics* vol 48a p 1.038

[50] Zotta V.K. *et al* 2024 Predictive modelling of JET baseline scenarios from DTE2 towards DTE3 *Proc. 50th EPS Conf. on Plasma Physics* vol 48a p 1.040

[51] Lombardo J. *et al* 2025 Interpretative TRANSP analysis of JET baseline scenario: performance dependence on plasma kinetic profiles *Nucl. Fusion* **65** 096009

[52] Romanelli M. and Orsitto F.P. 2021 On similarity scaling of tokamak fusion plasmas with different aspect ratio *Plasma Phys. Control. Fusion* **63** 125004

[53] Lin-Liu Y.R. and Stambaugh R.D. 2004 Optimum equilibria for high performance, steady state Tokamaks *Nucl. Fusion* **44** 548–54

[54] Orsitto F.P. *et al* 2024 High beta experiments on JET in preparation of JT-60SA *Proc. 50th EPS Conf. on Controlled Fusion and Plasma Physics* vol 48a p 1.051

[55] Challis C.D. *et al* 2015 Improved confinement in JET high β plasmas with an ITER-like wall *Nucl. Fusion* **55** 053031

[56] Mailloux J. *et al* 2014 Effect of 'baseline' and 'hybrid' operational parameters on plasma confinement and stability in JET with a Be/W ITER-Like wall *Proc. 41st EPS Conf. on Plasma Physics* vol 38f p O4.127

[57] Research Unit JT-60SA 2018 JT-60SA research plan v4.0 *Technical Report* (available at: www.jt60sa.org/wp/wp-content/uploads/2021/02/JT-60SA_Res_Plan-5.pdf)

[58] Joffrin E. *et al* 2005 The 'hybrid' scenario in JET: towards its validation for ITER *Nucl. Fusion* **45** 626–34

[59] Lerche E. *et al* 2025 Long pulse H-mode operation in JET-ITER like wall *Plasma Phys. Control. Fusion* **67** 95022

[60] King D.B. *et al* 2025 Operational challenges for long pulses on JET-ILW *Plasma Phys. Control. Fusion* **67** 85011

[61] Litaudon X. *et al* 2024 Long plasma duration operation analyses with an international multi-machine (tokamaks and Stellarators) database *Nucl. Fusion* **64** 015001

[62] Litaudon X. *et al* 2025 Investigating long-duration plasma operation with the international multi-machine database *Nucl. Fusion* submitted

[63] Maslov M. *et al* 2023 JET D-T scenario with optimized non-thermal fusion *Nucl. Fusion* **63** 112002

[64] Bachmann C. *et al* 2025 Engineering concept of the VNS - a beam-driven tokamak for component testing *Fusion Eng. Des.* **211** 114796

[65] Lerche E. *et al* 2016 Optimization of ICRH for core impurity control in JET-ILW *Nucl. Fusion* **56** 036022

[66] Goniche M. *et al* 2017 Ion cyclotron resonance heating for tungsten control in various JET H-mode scenarios *Plasma Phys. Control. Fusion* **59** 055001

[67] Lerche E. *et al* 2026 Heating D ions to optimal D-T fusion energies with ICRF waves *Nucl. Fusion* accepted (https://doi.org/10.1088/1741-4326/ae7986)

[68] Angioni C. 2025 The impact of tungsten and tungsten transport on H-mode plasmas, experiments and modeling *Nucl. Fusion* **65** 062001

[69] Dux R., Loarte A., Angioni C., Coster D., Fable E. and Kallenbach A. 2017 The interplay of controlling the power exhaust and the tungsten content in ITER *Nucl. Mater. Energy* **12** 28–35

[70] Field A.R. *et al* 2023 Peripheral temperature gradient screening of High-Z impurities in optimised 'hybrid' scenario H-mode plasmas in JET-ILW *Nucl. Fusion* **63** 016028

[71] Hobirk J. *et al* 2023 The JET hybrid scenario in deuterium, tritium and deuterium-tritium *Nucl. Fusion* **63** 112001

[72] King D., Challis C.D., Hobirk J. and Kappatou A. (JET Contributors) 2025 JET hybrid scenario development in D-T for impurity screening studies *Proc. 30th IAEA Fusion Energy Conf. (Chengdu, China)*

[73] Fajardo D. *et al* 2023 Analytical model for the combined effects of rotation and collisionality on neoclassical impurity transport *Plasma Phys. Control. Fusion* **65** 35021

[74] Solano E.R. *et al* 2023 L-H transition studies in tritium and deuterium–tritium campaigns at JET with be wall and W divertor *Nucl. Fusion* **63** 112011

[75] Hinton F.L. and Wong S.K. 1985 Neoclassical ion transport in rotating axisymmetric plasmas *Phys. Fluids* **28** 3082–98

[76] Saarelma S., Casper T., Chapman I.T., Huijsmans G.T.A., Kwon O., Lee J. and Loarte A. 2012 Edge stability analysis of ITER baseline plasma simulations *Nucl. Fusion* **52** 103020

[77] Snyder P. *et al* 2015 Super H-mode: theoretical prediction and initial observations of a new high performance regime for tokamak operation *Nucl. Fusion* **55** 083026

[78] Saarelma S., Challis C.D., Garzotti L., Frassinetti L., Maggi C.F., Romanelli M. and Stokes C. (JET Contributors) 2017 Integrated modelling of H-mode pedestal and confinement in JET-ILW *Plasma Phys. Control. Fusion* **60** 014042

[79] Frassinetti L. *et al* 2025 Low collisionality, peeling limited pedestals in JET-ILW: effect of density and isotope mass on pedestal structure, pedestal stability and pedestal prediction in deuterium and mixed deuterium/tritium plasmas *Nucl. Fusion* **65** 076028

[80] Frassinetti L. *et al* 2021 Role of the separatrix density in the pedestal performance in deuterium low triangularity JET-ILW plasmas and comparison with JET-c *Nucl. Fusion* **61** 126054

[81] Frassinetti L. *et al* 2023 Effect of the isotope mass on pedestal structure, transport and stability in d, d/t and t plasmas at similar β n and gas rate in JET-ILW type i ELMy H-modes *Nucl. Fusion* **63** 112009

[82] Kiptily V.G. *et al* 2024 Observation of alpha-particles in recent D–T experiments on JET *Nucl. Fusion* **64** 086059

[83] Molin A.D. *et al* 2024 Measurement of the gamma-ray-to-neutron branching ratio for the deuterium-tritium reaction in magnetic confinement fusion plasmas *Phys. Rev. Lett.* **133** 55102

[84] Mantica P. *et al* 2024 Detection of alpha heating in JET-ILW DT plasmas by a study of the electron temperature response to ICRH modulation *Nucl. Fusion* **64** 086001

[85] Mazzi S. *et al* 2022 Enhanced performance in fusion plasmas through turbulence suppression by megaelectronvolt ions *Nat. Phys.* **18** 776–82

[86] Kazakov Y.O. *et al* 2021 Physics and applications of three-ion ICRF scenarios for fusion research *Phys. Plasmas* **28** 020501

[87] Garcia J. *et al* 2024 Stable deuterium-tritium plasmas with improved confinement in the presence of energetic-ion instabilities *Nat. Commun.* **15** 7846

[88] Siena A.D. *et al* 2025 Understanding turbulence suppression in JET D–T plasma with highly energetic fast ions via global gyrokinetic GENE simulations *Nucl. Fusion* **65** 086019

[89] Varela J. *et al* 2025 Analysis of the linear and nonlinear stability of alfven eigenmodes and fish-bones in JET DT discharges: mode identification and shear flows generation *Nucl. Fusion* **65** 076044

[90] Ruiz J.R. *et al* 2025 Measurement of zero-frequency fluctuations generated by coupling between Alfvén modes in the JET Tokamak *Phys. Rev. Lett.* **134** 95103

[91] Ishizawa A., Poli E., Siena A.D. and Hahm T.S. 2025 Characterisation of turbulence suppression by fast-ion-alfvénic instability *Commun. Phys.* **8** 486

[92] Na Y.-S., Hahm T.S., Diamond P.H., Siena A.D., Garcia J. and Lin Z. 2025 How fast ions mitigate turbulence and enhance confinement in tokamak fusion plasmas *Nat. Rev. Phys.* **7** 190–202

[93] Kazakov Y., Garcia J., Nocente M. and Kiptily V. (JET Contributors) 2025 Insights from fast-ion physics studies on JET in support of JT-60SA and ITER rebaseline *Proc. 30th IAEA Fusion Energy Conf. Chengdu, China*

[94] Coelho R., Novara R. and Särkimäki K. 2025 Alpha particle generation and confinement in D-3He scenarios in JT-60SA *Nucl. Fusion* submitted

[95] Reman B.C.G. *et al* 2025 Velocity-space tomography of an MeV fast-ion tail generated by three-ion scheme ICRF heating at JET *Nucl. Fusion* **65** 076007

[96] Gerasimov S.N. 2024 Interaction of SPI pellets with plasma on JET and associated disruptions *Phys. Scr.* **99** 075615
[97] Sheikh U. 2021 Disruption thermal load mitigation with shattered pellet injection on the Joint European Torus (JET) *Nucl. Fusion* **62** 126043
[98] Jachmich S. *et al* 2022 Shattered pellet injection experiments at JET in support of the ITER disruption mitigation system design *Nucl. Fusion* **62** 026012
[99] Baylor L. *et al* 2021 Design and performance of shattered pellet injection systems for JET and KSTAR disruption mitigation research in support of ITER *Nucl. Fusion* **61** 106001
[100] Huang Z. *et al* 2024 Implementation of low temperature spectrometers for the JET high resolution thomson scattering diagnostic for disruption plasma measurements *Rev. Sci. Instrum.* **95** 073530
[101] Sheikh U. *et al* 2025 Impact of impurity seeding on shattered pellet injection mitigations on the joint european torus *Nucl. Fusion* **65** 036035
[102] Kong M. *et al* 2024 Interpretative 3d MHD modelling of deuterium SPI into a JET H-mode plasma *Nucl. Fusion* **64** 066004
[103] Kong M. *et al* 2025 3d MHD modelling of plasmoid drift following massive material injection in a tokamak *Nucl. Fusion* **65** 016042
[104] Piron L. *et al* 2024 Radiation asymmetry in JET disruption mitigation experiments with shattered pellet injection *Plasma Phys. Control. Fusion* **66** 085007
[105] Reux C. *et al* 2021 Demonstration of safe termination of megaampere relativistic electron beams in tokamaks *Phys. Rev. Lett.* **126** 175001
[106] Sheikh U. 2024 Benign termination of runaway electron beams on ASDEX Upgrade and TCV *Plasma Phys. Control. Fusion* **66** 035003
[107] Sheikh U. 2025 Multi-machine studies of low-z benign termination of runaway electron beams and extrapolation to iter *Proc. 30th IAEA Fusion Energy Conf. (IAEA FEC 2025)* p EX/C-2818
[108] Bergström H., Särkimäki K., Bandaru V., Skyllas M.M. and Hoelzl M. (JOREK Team) 2024 Assessment of the runaway electron load distribution in ITER during 3d MHD induced beam termination *Plasma Phys. Control. Fusion* **66** 095001
[109] Jepu I. *et al* 2024 Overview of damage to beryllium limiters by unmitigated disruptions and runaway electrons in the JET tokamak with metal walls *Nucl. Fusion* **64** 106047
[110] Lennholm M. *et al* 2025 Fusion burn regulation via deuterium tritium mixture control in the joint European torus *PRX Energy* **4** 23007
[111] Maslov M. *et al* 2018 Observation of enhanced ion particle transport in mixed h/d isotope plasmas on JET *Nucl. Fusion* **58** 076022
[112] Piron L. *et al* 2024 Innovative dud detection based on JET DT experience *Fusion Eng. Des.* **200** 114155
[113] Martin Y.R. and Takizuka T. and (the ITPA CDBM H-mode Threshold Database Working Group) 2008 Power requirement for accessing the H-mode in ITER *J. Phys.: Conf. Ser.* **123** 012033
[114] Loarer T. *et al* 2007 Gas balance and fuel retention in fusion devices *Nucl. Fusion* **47** 1112–20
[115] Widdowson A. *et al* 2021 Evaluation of tritium retention in plasma facing components during JET tritium operations *Phys. Scr.* **96** 124075
[116] Zayachuk Y., Catarino N., Likonen J., Rubel M. and Widdowson A. (JET Contributors) 2025 Time dependence of fuel retention in JET be plasma-facing components - comparison of single and multiple ITER-like wall campaigns *Nucl. Mater. Energy* **42** 101872
[117] Philipps V. *et al* 2013 Development of laser-based techniques for in situ characterization of the first wall in ITER and future fusion devices *Nucl. Fusion* **53** 93002
[118] Brezinsek S. *et al* 2013 Fuel retention studies with the ITER-Like Wall in JET *Nucl. Fusion* **53** 83023
[119] Widdowson A. *et al* 2025 Overview of fuel retention and recovery in JET deuterium-tritium operation *Nucl. Fusion* **65** 116036
[120] Matveev D. *et al* 2023 Tritium removal from JET-ILW after T and D–T experimental campaigns *Nucl. Fusion* **63** 112014
[121] Wauters T. *et al* 2022 Isotope removal experiment in JET-ILW in view of t-removal after the 2nd DT campaign at JET *Phys. Scr.* **97** 044001
[122] Zlobinski M. *et al* 2024 First results of laser-induced desorption - quadrupole mass spectrometry (LID-QMS) at JET *Nucl. Fusion* **64** 086031
[123] Matveev D. *et al* 2025 Analysis of fuel retention and recovery in JET with be-W wall *Nucl. Fusion* submitted
[124] Zlobinski M. *et al* 2025 In situ measurement of H, D, T retention in the JET tungsten divertor components–lessons learned for the ITER LID-QMS diagnostic *20th Int. Conf. on Plasma-Facing Materials and Components for Fusion Applications (PFMC-20)*
[125] Likonen J. *et al* 2014 First results and surface analysis strategy for plasma-facing components after JET operation with the ITER-like wall *Phys. Scr.* **T159** 014016
[126] Heinola K. *et al* 2017 Experience on divertor fuel retention after two ITER-like wall campaigns *Phys. Scr.* **T170** 014063
[127] Krat S. *et al* 2020 Comparison of erosion and deposition in JET divertor during the first three ITER-like wall campaigns *Phys. Scr.* **T171** 014059
[128] Almaviva S., Likonen J., Hakola A. and Karhunen J. 2025 Chemical analysis by laser induced breakdown spectroscopy of the poloidal cross-section of the JET divertor after its last D-T experimental campaign *Proc. 20th Int. Conf. on Plasma-Facing Materials and Components for Fusion Applications*
[129] Likonen J. *et al* 2025 First demonstration of laser induced breakdown spectroscopy using remote handling for in-vessel analysis of JET components *Nucl. Mater. Energy* **45** 102021
[130] Yi R. *et al* 2025 In-vessel and depth-resolved semi-quantitative analysis on hydrogen isotopes and wall materials in JET by LIBS operated on a remote handling arm *Nucl. Mater. Energy* **45** 102016
[131] Pitts R. *et al* 2025 Plasma-wall interaction impact of the ITER re-baseline *Nucl. Mater. Energy* **42** 101854
[132] Huber A. *et al* 2025 A laser-based diagnostic for in situ monitoring of fuel retention in ITER *Fusion Eng. Des.* **219** 115298